HHS Public Access

Author manuscript

Neuron. Author manuscript; available in PMC 2024 December 20.

Published in final edited form as:

Neuron. 2023 December 20; 111(24): 4024–4039.e7. doi:10.1016/j.neuron.2023.09.016.

Adult born granule cells facilitate remapping of spatial and non-spatial representations in the dentate gyrus

Sebnem N. Tuncdemir[1,2,+], **Andres D. Grosmark**[3,+], **Hannah Chung**[2], **Victor M. Luna**[1,2,++], **Clay O. Lacefield**[1,2], **Attila Losonczy**[3], **Rene Hen**[1,2,4]

[1]Departments of Psychiatry and Neuroscience, Columbia University, New York, NY 10032, USA

[2]Division of Systems Neuroscience, New York State Psychiatric Institute, New York, NY 10032, USA

[3]Department of Neuroscience, Mortimer B. Zuckerman Mind Brain Behavior Institute, Columbia University, New York, NY 10027, USA

Summary

Adult born granule cells (abGCs) have been implicated in memory discrimination through a neural computation known as pattern separation. Here, we examined how chronic ablation or acute chemogenetic silencing of abGCs affects the activity of mature granule cells (mGCs) using *in vivo* Ca^{2+} imaging. In both cases we observed altered remapping of mGCs. Rather than broadly modulating the activity of all mGCs, abGCs promote the remapping of place cells' firing fields while increasing rate remapping of mGCs representing sensory cues. In turn, these remapping deficits are associated with behavioral impairments in animals' ability to correctly identify new goal locations. Thus, abGCs facilitate pattern separation through the formation of non-overlapping representations for identical sensory cues encountered in different locations. In the absence of abGCs the dentate gyrus shifts to a state dominated by cue information, a situation that is consistent with the overgeneralization often observed in anxiety or age-related disorders.

Graphical Abstract

[4]Lead Contact: rh95@cumc.columbia.edu.

[+]Current Address: Department of Neuroscience, University of Connecticut Health, Farmington, Connecticut, 06032, USA

[++]Current Address: Alzheimer's Center at Temple, Lewis Katz School of Medicine, Temple University, Philadelphia, PA, 19140, USA

Author Contributions

S.N.T. and R.H. designed the research and wrote the paper. S.N.T. performed experiments and analyzed the data with assistance from A.D.G., H.C and C.O.L. V.M.L. conducted in vitro electrophysiological experiments. A.L. provided technical infrastructure and input to the manuscript.

Declaration of Interests: None declared

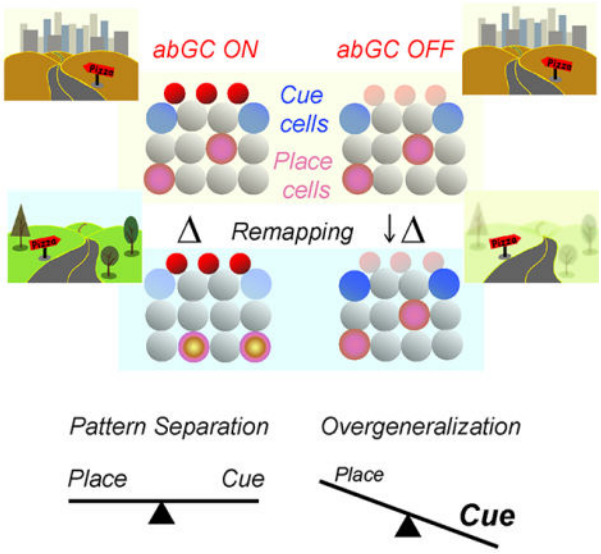

eTOC

Tuncdemir et al show that young adult-born hippocampal neurons are critical for mice's ability to discriminate between similar situations. In the absence of these young neurons, contextual representations are dominated by landmarks, a situation that is reminiscent of the overgeneralization often found in anxiety and age-related disorders.

Introduction

The hippocampal dentate gyrus (DG) exhibits a unique form of neural plasticity that results from continuous integration of adult born neurons, termed 'adult neurogenesis.' Four to 6 weeks after their birth, adult born granule cells (abGCs) exhibit increased synaptic plasticity and intrinsic excitability compared to mature granule cells (mGCs)[1–4]. Acute or chronic manipulations of abGCs during this period have demonstrated an important role for abGCs in hippocampus-dependent tasks involving behavioral pattern separation, such as the ability to discriminate between similar contexts or spatial locations[5–10]. Notably, the deficits resulting from impaired adult neurogenesis in animal models are consistent with low levels of neurogenesis as well as overgeneralization in patients with age-related memory impairments, anxiety, or depressive disorders[11–15]. It has therefore been suggested that abGCs play a role in this common endophenotype of these disorders[16,17].

The behavioral impact of abGCs has been proposed to result from their inhibitory modulation of mGCs resulting in increased sparseness of DG representations[18–22]. However, rather than broadly modulating mGCs in a uniform fashion, abGCs appear to dynamically interact with mGCs such that under different cortical inputs as engaged by distinct cognitive demands, abGCs may either inhibit or excite mGCs[23]. Thus, abGCs may engage different modulatory pathways to promote the formation of distinct mGC assemblies representing distinct contexts without interference from previously stored contextual memories.

A large proportion of principal neurons in all subfields of the hippocampus, including those in the DG, are considered place cells because they fire at specific locations corresponding to the position of an animal within an environment[24,25]. Collective activity of place cells in one environment is thought to form a cognitive map of this environment by integrating location-related sensory and self-motion information of the animal. A key property of place cells is the ability to change their preferred firing location or firing rate in response to changes in the environment, a process known as 'remapping'[26,27]. Remapping of place cells' firing properties in different environments is thought to underlie spatial and contextual discrimination by generating distinct representations of environments and behavioral experiences with varying levels of overlap with previously stored ones[28]. While remapping has been found in all hippocampal subregions, this feature is most consistent with the pattern separation function of the DG[16], a process by which similar input activity patterns are transformed into more distinct output patterns[29,30]. Pattern separation can be achieved by distinct DG populations responding to similar inputs ('global remapping') or by the same neurons changing their firing rates ('rate remapping'), resulting in increased discrimination of similar environmental inputs. While mGCs have been shown to exhibit global or rate remapping[31–35], how abGCs influence the remapping of mGCs in different contexts is not known. In addition, recent work has begun to characterize a functional diversity within the mGCs, whose activity are modulated by space or sensory cues (place cells and cue cells)[36–39]. These spatial and cue representations are distinct in their stability across different contexts as well as long-term dynamics[39], suggesting that different subpopulations of mGCs encode distinct contextual features. But, whether abGCs have a differential effect on the sensory cue versus place encoding mGCs or their remapping dynamics is not known.

Here, we have investigated how chronically ablating or chemogenetically silencing abGCs affects the activity of mGCs using *in vivo* 2-photon Ca^{2+} imaging. We find that inhibiting abGCs resulted in decreased remapping of mGCs, and behavioral impairments in animals' ability to correctly identify new goal locations.

Results

Adult born granule cells are necessary for the remapping of spatial representations

To investigate how abGCs influence DG activity, we first used a well-established method of focal X-irradiation to ablate adult hippocampal neurogenesis[40,41] and recorded Ca^{2+} dynamics in large populations of mGCs, a proxy for neuronal activity, in the mouse DG during head-fixed locomotion on a treadmill[9] (Figure 1A, S1A, STAR Methods). Ablation of neurogenesis was confirmed by the complete loss of doublecortin immunoreactive cells in the DG of X-irradiated mice (X-IR) compared to controls (Figure 1B) used for imaging. The specificity of spatial representations within the mGC population were examined during three consecutive exposures to two identical and then a different context[9] (STAR Methods). We tracked the same mGCs[42,43] and were able to cross-register substantial number of mGCs active in the same fields of view in both control and X-IR mice during sequential exposures to either same (A-A') or different (B) contexts (Figure S1B–D).

We focused on the mGCs that showed spatially tuned activity in at least one of the three sessions and compared the similarity of their spatial fields between two sequential exposures to either same (A-A') or different (A'-B) contexts. Both groups of mice displayed stable spatial maps when they were exposed to the same context and distinct maps when exposed to different contexts (Figure 1C,D). Strikingly, X-IR mice showed markedly lower levels of reorganization of mGC spatial firing compared to controls in a different context (Figure 1C,D). Accordingly, spatially tuned mGCs displayed high correlation of their tuning curves in both controls and X-IR mice in the same context, whereas X-IR mice displayed significantly higher correlation of tuning curves compared to controls in different contexts (Figure 1E). In addition to responses of individual mGCs, we were also interested in the population level changes of spatial coding in response to chronic ablation of neurogenesis. Hence, we used a Bayesian decoder[44] to predict the position of the mice in the same (A) or different (B) contexts from the neural activity in A' using granule cells cross-registered in all sessions (STAR Methods). The decoder error, calculated as the median of the absolute difference between predicted and actual positions, was similar in both groups of mice when position was predicted in the same context (A-A'). But, the X-IR mice showed consistently lower prediction errors compared to controls in different contexts (A'-B, Figure 1Fii) suggesting impaired context discrimination in X-IR mice compared to controls (Figure 1Fiii).

We confirmed that the differences in tuning correlation or decoder prediction error in different contexts between control and X-IR mice did not result from the differential cross-session registration of cells due to differences in the stability of fields of view, as assessed by the similar fraction of all active or only spatially tuned mGCs imaged in control and X-IR mice (Figure S1D). Similarly, the fraction of all or only spatially tuned mGCs cross-registered in contexts A or B were comparable between different groups (Figure S1E,F). Additionally, the population vector correlations of the Ca^{2+} event rates of mGCs in X-IR mice at all positions in different contexts (A vs B) were increased compared to controls (Figure S1G,H), consistent with a role for adult neurogenesis in promoting the remapping of spatial representations during exploration of different contexts.

X-irradiation permanently blocks adult hippocampal neurogenesis; hence, we used chemogenetics to acutely and selectively silence the activity of 4-week-old abGCs because this time point is within the hyperplastic phase during which they are thought to most strongly influence behavior[6,7]. We crossed a conditional hM4Di[21,45] mouse line with abGC specific Ascl1-CreERT2 knock-in mice[46,47] (referred to as $Ascl^{CreER}Di^{F/F}$ and compared to *Cre* negative $Di^{F/F}$ littermates), and investigated the spatial activity in mGCs after acute inhibition of 4-week-old abGCs (Figure 2A). We confirmed the efficacy of this strategy was confirmed in acute slice preparations (Figure S2Ai–iv) and ruled out a potential reduction in abGC numbers in virus injected compared to the contralateral hemispheres[48,49] (Figures 2B, S2B).

Like in the previous experiment, we compared neural activity during two sequential exposures of either identical or different contexts. The first session in context A was the baseline, and clozapine-N-oxide (CNO) was *i.p* injected 30-mins before re-exposure to A (A') and context B in both groups of mice to silence abGCs (Figure 2A, STAR Methods).

We chose this injection scheme so that the abGCs are offline both during the second exposure to familiar and novel contexts akin to those in chronic ablation experiments, but also to have a baseline session in the first exposure to Context A, enabling detection of differences of abGC manipulation in the same populations of mGCs. The injection of CNO did not have an effect on the spatial firing stability in the same contexts in both groups of mice (Figure 2C,D). However, acute inhibition of 4-week-old abGCs in $Ascl^{CreER}Di^{F/F}$ mice resulted in impaired remapping in different contexts (Figure 2C,D). We note that the activity correlation between exposures to different contexts (A'-B) were elevated in the chemogenetic experiments due to an enrichment of activity in the middle position in Context A' corresponding to odor delivery via air puff that was partially preserved in B despite different identities of odorants (Figure 2C,D). This effect was absent and accompanied with lower correlation in the controls of the X-IR experiment due to ambient delivery of different odors (Figure 1C,D). However, similar to the differences between controls and X-IR mice: $Di^{F/F}$ controls did remap their firing fields between contexts A and B whereas this ability was reduced in $Ascl^{CreER}Di^{F/F}$ mice. Again, mGCs with spatially tuned activity in at least one of the contexts A, A' or B (same selection criteria as above) displayed high correlation of their tuning curves in both $Di^{F/F}$ and $Ascl^{CreER}Di^{F/F}$ mice in the same context (A-A'), whereas $Ascl^{CreER}Di^{F/F}$ mice displayed significantly higher correlation of tuning curves compared to controls in different contexts (A'-B, Figure2E). Bayesian decoders used to predict the position of the mice in the same (A) or different (B) contexts from the neural activity in A' using granule cells cross-registered in all sessions also reflected remapping impairments in CNO-treated $Ascl^{CreER}Di^{F/F}$ mice compared to CNO-treated controls (Figure 2Fi,ii), resulting in significantly lower context discrimination in $Ascl^{CreER}Di^{F/F}$ mice compared to $Di^{F/F}$ controls (Figure 2Fiii).

We also investigated whether chemogenetically silencing a similar number of mature GCs would have a similar or different effect on the remapping of mGC representations in different contexts. We took advantage of the fact that after a critical period of 4–6 weeks, abGCs become functionally indistinguishable from mature GCs[1,6,47,50]. Therefore, we silenced an older population of abGCs that were 7 to 8-weeks-old, using the same tamoxifen inducible $Ascl^{CreER}Di^{F/F}$ genetic line and observed that specifically silencing abGCs at this time point does not impair remapping of representations in different contexts (Figure S2C–F). Further, the effect size of Control - X-IR and $Di^{F/F}$ - $Ascl^{CreER}Di^{F/F}$ cohorts were comparable when the abGCs are 4 but not 7–8 weeks old (Figure S2G), indicating that the observed impairments in both mouse models likely result from cell autonomous effects of abGCs on the DG circuitry rather than non-specific effects of irradiation[51]. Hence, our results with chronic ablation of adult hippocampal neurogenesis and acute silencing of abGCs reveal that 4-week-old abGCs transiently facilitate neural discrimination of different contexts by promoting the remapping of mGCs' spatial receptive fields. These results are consistent with previous studies showing the existence of a critical period for abGC function[6,7,52].

Adult born granule cells modulate remapping of mature granule cells without large changes in global activity levels or spatial tuning

Next, we examined the underlying mechanisms by which abGCs promote spatial coding flexibility. Numerous studies have proposed that abGCs inhibit the activity of the mGC population[18,21,22]. However, we recently demonstrated a functional heterogeneity in the way abGCs modulate mGCs[23] in addition to diverse response properties of mGCs to spatial and non-spatial information[39]. Notably, abGCs do not uniformly inhibit all mGCs, but depending on the incoming afferents from the lateral or medial entorhinal cortex, abGCs can either inhibit or excite mGCs[23]. Here, we found that the fraction of total active (with at least 1 Ca^{2+} transient) and spatially tuned mGCs did not significantly change after chronic ablation (Figure 3A) or acute inhibition of abGCs (Figure 3D). In both models, there were no significant differences in overall mean Ca^{2+} event rates within a session per animal (Figure 3B, E) and spatially tuned neurons had comparable spatial information content[53] (Figure S3A,B). While cumulative distributions of event rates in all mGCs were comparable in controls and X-IR mice (inset in Figure 3B), there was a small but significant elevation in Ca^{2+} rates in $Ascl^{CreER}Di^{F/F}$ compared to $Di^{F/F}$ mice both in baseline and after CNO injections (inset in Figure 3E), which may point to a possible leak in this transgenic line. Nevertheless, we found that the normalized rate differences in baseline and CNO injected sessions were comparable in $Ascl^{CreER}Di^{F/F}$ compared to $Di^{F/F}$ mice (Figure S3C). In addition, similar fractions of neurons across experimental and control groups imaged during Context A' maintained their spatial tuning when cross-session registered to cells in same or different contexts in both mouse models (Figure S3D,E). Instead, the relationship of individual mGC's Ca^{2+} event rates with their remapping index, a measure of the difference in correlations between similar contexts and different contexts[34], were consistently different from controls in both models of chronic X-IR ablation or acute inhibition of abGCs. The distribution of the Ca^{2+} event rates of spatially tuned mGCs revealed that the high firing rate cells in X-IR mice showed the most pronounced deficit in context selectivity (as defined by their low remapping index) compared to controls (Figure 3C). However, the relationship between the remapping index and mean rates was not statistically different between mGCs in $Ascl^{CreER}Di^{F/F}$ mice compared to $Di^{F/F}$ controls (Figure S3F), suggesting that the effect of abGC is not solely on cells that have a high-firing rate. Instead, tracking how transient inhibition of abGCs changes both Ca^{2+} event rates and the remapping responses of single neurons before and after injection of CNO revealed that mGCs most sensitive to the influence of abGCs in $Ascl^{CreER}Di^{F/F}$ mice were those that were disinhibited and exhibited the least remapping between contexts A-B compared to controls (Figure 3F). These differences were not due to independent differences in cross-session stability (*r*AA') or remapping (*r*AB, *r*A'B, data not shown). Taken together, these results indicate that chronic ablation and acute inhibition of abGCs do not influence every mGC evenly, suggesting a functional heterogeneity in the way abGCs engage different modulatory pathways to promote the formation of distinct spatial maps by mGCs. Our results also reveal that under normal conditions, the subpopulation of mGCs that are selectively inhibited by abGCs display increased context selectivity.

Adult born granule cells control remapping of mGCs with spatial and non-spatial responses

We have recently described a functional heterogeneity in mGCs in response to sensory cue and self-motion information during spatial navigation[39]. Cue responses in single neurons were stable for long periods of time while place cells were more context selective[39]. To investigate how abGCs affect these two responses, we first revisited our initial experiments with different contexts (Figures 1–2) where multiple sensory features are used to define these contexts. We divided the spatially tuned population for subsequent analyses based on the position of their spatial fields during the context discrimination task (STAR Methods). Presumed '*place'* cells were defined as mGCs with peak Ca^{2+} event rates outside of the affixed tactile cues on the treadmill belt during the second exposure to context A, while '*cue*' cells were defined as mGCs with peak activity within the boundary of the tactile cues on the belt (Figure S3G,J). The high firing rate place cells in X-IR mice (Figure S3H) and the most disinhibited place cells in $Ascl^{CreER}Di^{F/F}$ mice (Figure S3K) showed the most pronounced deficit in remapping index. This relation between remapping and activity was not observed in place cells that were not inhibited by abGCs or cells with a tuning field near the tactile cues (Figure S3I,L,M,N) suggesting a differential impact of abGCs on the remapping dynamics of a subset of place encoding mGCs during context discrimination.

We then investigated whether abGCs manipulations affect tuning dynamics of the sensory representations by using a task in which an olfactory cue was omitted or shifted one-quarter of the track length in a subset of lap crossings interleaved throughout the session (Figure 4A). By controlling the administration of sensory cues and their association with locations on the treadmill track, we aimed to better isolate 'cue' and 'place' cell populations of mGCs. Like in controls (data previously reported in[39]), in X-IR mice sensory cue responsive mGCs remapped their firing position to match the new location of the odor in cue-shift laps (Figure 4B, middle) and exhibited reduced activity in cue-omitted laps, while the representation of the track by place encoding mGCs were not affected by the absence of odor cue (Figure 4B, right). In both controls and X-IR mice, cue cells showed higher averaged spatial information, had more consistent spatial firing between the first and the second half of each session, and displayed earlier in-field onset firing than the place cells (Figure S4A–C). However, compared to controls, X-IR mice displayed increased Ca^{2+} event rates both at the more frequent middle odor cue location and when the odor cue was presented at the infrequent "shift" location (Figure 4SD,E) together with significant changes of activity in the positions preceding and following the odor-cue corresponding to the non-cue related place cells, but not at positions corresponding to the invariant tactile lap cue (Figure S4F). Additionally, while in control mice mGCs displayed smaller responses when the cue cells remapped upon shifting the cue to another location (Figure 4C); in X-IR mice the cue responses during the shift laps were comparable to the more frequent middle cue laps (Figure 4D). This resulted in reduced spatial modulation of cue cells in X-IR mice compared to controls (Figure 4E). We have previously proposed that mGCs that stably respond to the same sensory cue regardless of location on the belt did not encode spatial location with a different reference frame but were indeed representing non-spatial information[39]. However, the rates of these cue mGCs was dependent on the global reference frame[54], since cue cells had different amplitudes when cues were presented at different locations. Here we show

that loss of abGCs leads to a reduction in the spatial modulation of cue mGCs' rates and reduced rate remapping in response to cues encountered in different locations. In agreement with the changes in remapping of cue responses in X-IR mice, population correlations of firing rates of mGCs on middle cue and cue shifted laps was elevated at the odor cue location compared to controls (Figure 4F). These changes in mGC activity were limited to the cue responses as the population correlations in response to omitting the cue were comparable between controls and X-IR mice (Figure 4G). Thus, the absence of abGCs alters the remapping of cue cells by reducing the influence of spatial location on cue responses. Taken together, our results suggest that abGCs facilitate differential encoding of different contexts by modulating the rate remapping of the cue cells when sensory cues are presented at different locations and global remapping of the tuning fields of place cells representing the animal's location in between these cues.

Adult born granule cells control long-term stability of DG representations

We then took advantage of the chronic nature of our imaging setup and sought to characterize the influence of neurogenesis on the long-term stability of the GC subpopulations. We used the spatial cue task described above (Figure 4) to examine the responses of individual GCs on subsequent sessions with 1 hour between sessions or 1 week later (Figure 5A). We first used Bayesian decoding to infer how well we could predict the mouse's location on the same day or one week later using neural data from the first session on day 1 (Figure 5Bi). While the predicted position error was similar in both groups of mice when position was predicted using the cells found on sessions from the same day, the X-IR mice showed consistently lower prediction errors compared to controls when the position on day 7 is predicted using neural data from the first session on day 1 (Figure 5Bii). This resulted in a higher stability index in X-IR mice compared to controls (Figure 5Biii).

We then examined cue and place populations separately to determine the relative influence of abGCs on these two populations. In control mice, cross-registered odor cue cells fired reliably to the same olfactory cue after 1 week, while the correlations in the activity of place cells after 1 week were significantly lower (Figure 5C). In X-IR mice however, place cells displayed reduced remapping from day-1 to day-7 compared to controls, as measured by increased correlation of their tuning curves (Figure 5C). Further, when we examined how cue representations change over time, we observed an increase in their responses to the cue shifts 1 week later in X-IR mice compared to controls, as measured by population correlations of firing rates of mGCs on middle cue versus shifted cue laps (Figure 5D). This is consistent with higher levels of cue cell activity in the cue shifted laps relative to the middle cue laps after 1 week in X-IR mice (Figure 5E), indicating a reduction in rate modulation in response to odor cues. Thus, both across time and in different contexts, abGCs increase remapping of cue and place cells, whereby they promote rate modulation of cue cells and increase the flexibility of place cells' firing field location.

Behavioral impact of impaired mGC remapping in the absence of adult born granule cells.

Lastly, we explored the behavioral consequences of the neural impairments observed in the absence of abGCs. To this end, we used a hippocampus-dependent head-fixed goal-oriented learning (GOL) task (Figure 6A) in which operant water rewards are delivered

at a fixed treadmill location and mice learn to lick selectively near this hidden reward location[43,55–59]. We introduced a 'reversal' session after two 'training' sessions in which the location of the reward zone but not the local cues on the belt are changed, based on freely moving behavioral tasks that suggest a specialized role for abGCs during learning novel or conflicting goals arising in familiar situations[41,60–62] (STAR Methods). We found that chronically ablating abGCs impairs the reversal but not the initial learning of the reward location (Figure 5SA,B–C), as measured by the spatial distribution of lick behavior in the anticipatory goal region (Figure 6C) and at the goal location (Figure6D) without altering the overall licking behavior (Figure 6E). Thus, our results recapitulate previous studies and show that chronically ablating abGCs impairs the reversal but not the initial learning of a reward location in a head-fixed behavioral task[41,60–62].

In agreement with our previous findings (Figures 4 and 5), suppressing abGCs promotes stronger cue-elicited responses (here reward also acts as a cue, Figure 6G) and increased stability of place responses in the area of the treadmill before the reward delivery (anticipatory lick zone, Figure 6H). These differences between controls and X-IR mice were specific to the reversal session since the activity of mGCs in controls and X-IR mice were comparable in training Sessions 1 and 2 (Figure S5D–F). Further, we found that the control mice showed a negative correlation between the similarity of mGC activity in the anticipatory zone and anticipatory lick rates, and that this correlation was absent in the X-IR group (Figure 6I). Thus, our behavioral experiments suggests that an increase in remapping before reward delivery is correlated with the task performance. However, in all X-IR mice the population similarity in the anticipatory region remained elevated indicating reduced remapping (Figure 6I). Thus, our behavioral experiments suggests that an increase in remapping in representations in the positions before reward delivery is correlated with the task performance in controls compared to X-IR mice. Collectively, these findings demonstrate specific impairments in the representations as a result of abGC loss of function, whereby cue responses became dominant at the expense of flexible place responses in the absence of abGCs, in turn impairing pattern separation and animals' ability to flexibly adapt to new goal locations.

Discussion

Using *in vivo* two-photon calcium imaging we investigated how distinct representations of contextual features are impacted by loss of abGCs function and found decreased remapping of contextual representations resulting from ablation or inhibition of abGCs that is not due to a broad disinhibition of mGCs or a global change in their spatial tuning. Instead, the functional impact of abGCs is dependent on the specific contextual features the mGCs encode, such as information about the goals or sensory cues within an environment. Taken together, our work provides a novel framework by which abGCs promote pattern separation: abGCs promote remapping of the firing field locations of place cells (Figure S6A) and facilitate the rate remapping of cue cells (Figure S6B). Thus, the influence of abGCs on the remapping properties of spatial and non-spatial responses likely contributes to pattern separation by allowing the formation of distinct engrams when the same cues or other salient features such as rewards are encountered in different locations (Figure S6C).

Adult born granule cells modulate mGC representations

The ability of abGCs to control remapping depending on the type of information mGCs encode, likely amplify their influence despite their small number within DG[63]. Previous *in vivo* studies showed that genetically identified abGCs are highly excitable and display a lower spatial tuning specificity than mGCs, features which may be ill suited for coding spatial information[9,22]. Here, we extend these observations and provide evidence in support of a modulatory rather than a direct role of abGCs in flexible encoding of different contextual features. Our findings reveal that chronic or acute manipulations of abGCs do not impair initial encoding of contextual features, population level mean firing rates or spatial tuning properties. Hence, while the details of the contextual features such as the sensory cue and self-motion information can emerge and be refined during cognitive map formation without abGCs, the ability of the DG network to form new representations of novel contexts or changes in goal contingencies is impaired.

Aside from pattern separation, our finding that abGCs promote remapping of mGC is also compatible with their previously proposed roles in increasing memory capacity[64] or forgetting[65]. By modulating remapping of the cue cells that encode the same sensory cue with varying rates when the cue is presented at different locations (Figure 4), abGCs increase the impact of spatial location on cue responses resulting potentially in increased memory resolution and discrimination in downstream regions[64]. On the other hand, abGC dependent facilitation of the remapping of place cells (Figure 5) may result in a decrease in the successful retrieval of old memories (i.e. 'forgetting')[65,66]. Mechanistic and microcircuit-based studies will be necessary to resolve whether abGCs have primarily a modulatory role[21–23,67] or whether they also are independent broadly tuned encoding units[9,22,64]and how these properties contribute to remapping and memory discrimination.

Origins of abGC mediated remapping in the DG

Extensive prior work has proposed that the inputs from the entorhinal cortex trigger hippocampal remapping[26,28]. The main long-range excitatory inputs of the mGCs come from the medial and lateral entorhinal cortices (MEC and LEC, respectively)[68]. The MEC is thought to prominently encode self-motion information, while the LEC is thought to primarily represent information about sensory cues[69,70]. Global remapping of CA1/3 place cells, whereby place cells change their preferred firing location, is strongly associated with the activity of the grid cells in the MEC[71–73]. Our finding that abGCs inhibit a subpopulation of place cells that exhibit global remapping (Figures 3–S3) suggests that this abGC-mediated inhibition is necessary for the emergence of new place fields possibly as a result of new MEC grid cells inputs (Figure S6A). In keeping with these findings, abGCs have been shown to inhibit the activity of mGCs both via local interneurons[20,74] and possibly monosynaptically[23].

The circuit mediating the impact of abGCs on the remapping of cue encoding mGCs likely involves the LEC. Notably, a recent study has demonstrated specific impairments in hippocampal rate remapping upon lesions of the LEC[75]. Furthermore, abGCs receive strong monosynaptic inputs from the LEC during their hyperplastic phase[76,77], which can in turn reduce the activity of mGCs in response to LEC inputs[23]. Hence, we suggest that one

function of abGCs is to modulate LEC inputs to cue cells either via interneurons[19,20,74] or via direct monosynaptic inhibition of cue cells through group II metabotropic glutamate receptors[23]. This inhibition may promote rate modulation of the cue cells induced by changes in their location (Figures 4–5) to promote the formation of distinct 'rate modulated' traces for the same cues encountered in different locations (Figure S6B).

Neurogenesis and overgeneralization

The remapping impairments in the mGCs resulting from the loss of abGCs likely influence the propagation of information in the next stages of the hippocampal circuit during formation of cognitive maps used to guide behavior. Subsequent hippocampal areas such as the CA3 recurrent attractor network may receive conflicting cue and locomotion-based information from the DG resulting in errors in an animal's estimated position (Figure 6). Future studies examining how these specific features are altered in subsequent stages of the hippocampal circuit in the absence of abGCs will be necessary to clarify their role in the integration of sensory cue and spatial information during cognitive map formation. The phenotype displayed by the X-IR and $Ascl^{CreER}Di^{F/F}$ mice may be characterized by an overreliance on salient features such as cues or goals at the detriment of spatial locations when encoding novel environments (Figure S6C). In turn, this phenotype is reminiscent of the overgeneralization that is often observed in age related disorders such as mild cognitive impairment or in anxiety disorders such as PTSD[11,12,14,17,78]. For example, a patient who developed PTSD following 9/11 may display an exaggerated fear response at the sight of a plane or a tower because of an inability to separate the present safe situation from the past traumatic experience. Interestingly, there is some evidence for low levels of neurogenesis as well as overgeneralization in patients with age-related memory impairments, anxiety, or depressive disorders[13,15]. It will therefore be interesting to investigate whether strategies aimed at modulating DG function either indirectly by stimulating neurogenesis or directly by modulating the activity of mGCs may be beneficial for the treatment of patients who display this form of overgeneralization.

Limitations of the Study

The classification of mGC populations into place and cue encoding cells reflects their associated spatial and non-spatial responses on a treadmill belt repeatedly traversed in a fixed sequence, and therefore we cannot rule out the possibility of a distinct activity profile in freely foraging animals[79]. Second, it may be the case that the place cells in our study may jointly code for space as well as other environmental features, as recently reported in another study in which freely moving mice display multiplexed encoding of objects and space[38] by integrating self-motion information referenced to a landmark (such as the invariable lap boundary cue in our task). Finally, cells classified as place cell in our study could also reflect temporal sequences of activation[80] in between prominent non-spatial stimuli (odor cue and lap cue) on a linear track. Despite these caveats, a large body of in vivo hippocampal work has shown that there is a diversity of hippocampal encoding dynamics associated with distinct features of the environment and of behavior[81,82]. For instance, time and experience independently affect rate and spatial tuning of CA1 place cells[83,84] and replay of spatiotemporal sequences in CA1 occurs in a non-uniform manner not easily explained by these same parameters[44,85,86]. The mechanisms underlying these different

hippocampal representations remain unknown and may involve recruitment of unique neural pathways. While we have not looked at replay, our results suggest that abGCs contribute to representational drift[83,84,87–89] since in their absence we observe reduced drift when mice are re-exposed to the same context after 7 days (Figure 5). It will therefore be important in future experiments to investigate specifically the impact of abGCs on representational drift and replay dynamics and whether these may explain our remapping results.

Star Methods

Resource Availability

Lead Contact—Further information and requests for resources and reagents should be directed to and will be fulfilled by the lead contact Rene Hen (rh95@cumc.columbia.edu).

Materials availability—This study did not generate new unique reagents.

Data and code availability—All data reported in this paper will be shared by the lead contacts upon request. This paper does not report original code. Any additional information required to reanalyze the data reported in this paper is available from the lead contact upon request.

Experimental Model and Study Participant details

Mice—All procedures were conducted in accordance with the U.S. NIH Guide for the Care and Use of Laboratory Animals and the Institutional Animal Care and Use Committees of New York State Psychiatric Institute and Columbia University. Adult male and female C57BL/6J mice were supplied by Jackson Laboratory for irradiation experiments, *Ascl-creERT2*$^{+/-}$ were purchased form Jackson Laboratory and bred in house with *loxP-stop-mCherry-loxP-hM4Di* mice to obtain male and female Cre^{-} and Cre^{+} littermates from heterozygote breedings. At least three separate cohorts of mice were run for all imaging experiments. A sperate cohort of *Ascl-creERT2*$^{+/-}$ mice was crossed to TdTomato$^{F/F}$ mice to test whether AAV injections reduce the number of abGCs. Mice were housed in a vivarium grouped 2–4 mice/cage enriched with running wheels, maintained on a 12-hour light cycle and used at 8–10 weeks of age. To activate Cre-recombinase activity, mice at 8–10 weeks of age were administered *i.p.* tamoxifen injections for 5 consecutive days (100 mg kg^{-1} suspended in corn oil). The 5th day was designated post-induction day 0. Imaging experiments were conducted 4–8 weeks later. For in vivo silencing of abGCs in *Ascl*^{CreER} *hM4Di* $^{F/F}$ compared to *Cre* negative *hM4Di* $^{F/F}$ littermates CNO was dissolved in 100% dimethyl sulfoxide (DMSO) and diluted with 0.9% saline to a final concentration of 5 μM CNO and 0.001% DMSO. 30 minutes before the imaging session all mice received 5 mg kg^{-1} CNO diluted in 0.9% saline, administered by *i.p.* Experiments were conducted during the light portion of the cycle. Food and water were available *ad libitum* until the beginning of the experiment, when they were placed under controlled water supply and maintained at >85% of their pre-deprivation weight over the course of imaging experiments.

Method details

Focal X-irradiation—Hippocampal irradiation was conducted as previously described[6,41]. Briefly, after ketamine (105 mg/kg, i.p.) and xylazine (7 mg/kg, i.p.) anesthesia, 8–10-week-old mice were placed in a stereotaxic frame, and cranial irradiation applied directly above the hippocampus in order to block hippocampal neurogenesis while leaving other neurogenic regions intact. There was a 3.22 × 11-mm window above the hippocampus in a lead plate that otherwise shielded the entire body and allowed for focal Xray application. X-rays were filtered using a 2 mm Al filter, the corrected dose rate was approximately 1.8 Gy per min and the source to skin distance was 30 cm. A cumulative dose of 5 Gy was given over the course of 2 minutes and 47 seconds on 3 days with 2–3 days between each X-ray session. Control mice did not receive radiation, but were housed, anesthetized, and transported with irradiated mice throughout the experiment. Injection and implantation were performed 8 weeks later.

Surgery—Dentate gyrus virus injection and imaging window implantation surgeries were performed as described previously[9,39]. For all surgical procedures, mice were anesthetized with 1.5% isoflurane at an oxygen flow rate of 1 L/min, and head-fixed in a stereotactic frame (Kopf Instruments, Tujunga, CA). Eyes were lubricated with an ophthalmic ointment, and body temperature maintained at 37°C with a warm water recirculator (Stryker, Kalamazoo, MI). The fur was shaved and incision site sterilized prior to beginning surgical procedures, and subcutaneous saline and carpofen were provided peri-operatively and for 3 days post-operatively to prevent dehydration and for analgesia. Mice were unilaterally injected with recombinant adeno-associated virus (rAVV) carrying the GCaMP6s or GCaMP7s transgenes (pAAV.Syn.GCaMP6s.WPRE.SV40 or pGP-AAV-syn-jGCaMP7s-WPRE) purchased from Addgene (viral preps #100843-AAV1, 104487-AAV1) with titers of $1–5\times10^{12}$ in dorsal dentate gyrus using a Nanoject syringe (Drummond Scientific, Broomall, PA). Unilateral injection coordinates for dorsal DG were −2 mm AP, −1.5 mm ML, and −1.8, −1.7, −1.55 mm DV relative to the cortical surface 30 nL of 1:3 diluted virus was injected at each DV location in 10 nL increments. Mice were allowed to recover for 3 days and then were unilaterally implanted with an imaging window and stainless-steel head-post for head fixation. Imaging windows were constructed by adhering 2 mm diameter, 2.3 mm long stainless-steel hypodermic tubing (Ziggy's Tubes and Wires Inc, Pleasant Hill, TN) to 2 mm diameter glass coverslips (Potomac Photonics, Halethorpe, MD). A 2 mm diameter craniotomy was made centered on the previous injection site with a taper pointed-drill (Henry Schein Inc, 9004367) and dura was removed with micro curette (FST, 10080–05). The overlying cortex was gently aspirated to reveal capsular fibers with continuous irrigation with ice cold aCSF solution and bleeding was controlled with a collagen gel sponge (Avitene). Under minimal bleeding, a 30g blunt syringe was used to gently aspirate capsular and CA1 alveus fibers with white appearance and CA1 pyramidale and moleculare with pink appearance until vasculature of the hippocampal fissure became visible (under bright light with low bleeding). The cannula, attached to the stereotactic handle, was then gently lowered into the craniotomy and affixed to the skull using dental cement (Unifast Trad powder and LC light cured acrylic UV, Henry Schein).

In vitro electrophysiology—Chemogenetic manipulation of abGCs using *Ascl1*^{CreER} *hM4Di* $^{F/F}$ mice was confirmed by using *in vitro* whole-cell current clamp recordings on mGCs in slice preparations as described previously[23]. Briefly, after 4–8 weeks post-tamoxifen inductions, mice were anesthetized by isoflurane inhalation, decapitated, and brains rapidly removed. DG slices (350μm) were cut on a vibratome (Leica VT1000S) in ice cold partial sucrose artificial cerebrospinal fluid (ACSF) solution (in mM): 80 NaCl, 3.5 KCl, 4.5 MgSO4, 0.5 CaCl2, 1.25 H2PO4, 25 NaHCO3, 10 glucose, and 90 sucrose equilibrated with 95% O2 / 5% CO2 and stored in the same solution at 37°C for 30 minutes, then at room temperature until use. Recordings were made at 30–32°C (TC324-B; Warner Instrument Corp) in normal ACSF (in mM: 124 NaCl, 2.5 KCl, 1 NaH2PO4, 25 NaHCO3, 20 glucose, 1 MgCl2, 2 CaCl2). Whole-cell recordings (−70 mV) were obtained using a patch pipette (4.5–6.5 M) containing (in mM): 135 KMethaneSulfate, 5 KCl, 0.1 Na-EGTA, 10 HEPES, 2 NaCl, 5 ATP, 0.4 GTP, 10 phosphocreatine (pH 7.2; 280–290 mOsm). Recordings were made without correction for junction potentials. Granule cells were visualized and targeted via infrared-differential interference contrast (IR-DIC; 40x objective) optics on an Axioskop-2 FS (Zeiss). For perforant path stimulation, a concentric bipolar stimulating electrode (FHC) controlled by a stimulus isolator (ISO-flex, AMPI Instruments) was positioned on the DG molecular layer (triggered at 0.04 Hz). Perforant path inputs were stimulated at 40 Hz (20 pulses every 25 ms) at the lowest stimulation intensity to elicit 100% responses in mGCs. Current and voltage signals were recorded with a MultiClamp 700B amplifier (Molecular Devices, USA), digitized at 5–10 kHz, and filtered at 2.5–4 kHz. Data were acquired and analyzed using Axograph (Axograph Scientific, Sydney, Australia). Evoked synaptic responses were quantified by calculating the AUC (cumulative area above (+) and below (−) the baseline in mV s).

Immunohistochemistry—Brains were fixed by transcardiac perfusion with 4% paraformaldehyde (PFA)/phosphate-buffered saline (PBS) solution followed by a 1-h post-fixation on ice with 4% PFA/PBS solution. Brains were rinsed with PBS and cryoprotected by using 30% sucrose/PBS solution overnight at 4 °C. Tissues were embedded in Tissue Tek, frozen on dry ice, and cryosectioned at 30 μm thickness. Sections for immunohistochemistry analysis were processed using 1.5% normal goat serum (NGS) and 0.1% Triton X-100 in all procedures except washing steps, where only PBS was used. Sections were blocked for 1 h, followed by incubation with the primary antibodies overnight at 4 °C. Cryostat tissue sections were stained with the following primary antibodies: goat anti-Doublecortin (E-6, 1:500, Santa Cruz Biotechnology), chicken anti-EGFP (1:1000, Aves labs), rabbit anti-DsRed (1:500, Milllipore). Secondary antibodies conjugated with Alexa fluorescent dyes 488, and 594 (Jackson Immunoresearch) raised from the same host used for blocking serum were applied for 1 h at room temperature for visualizing the signals. Nuclear counterstaining was performed with 100 ng/mL 4,6-diamidino-2-phenylindole (DAPI) solution in PBS for 5 minutes. Fluorescent images were captured using a confocal scanning microscope (Leica TCS SP8, Leica Microsystems Inc.) equipped with three simultaneous PMT detectors Fluorescence from Alexa 488 was excited at 488 nm and detected at 505–550 nm, and fluorescence from Alexa 594 was excited at 552 nm and detected at 600–650 nm. For 488- and 552-nm excitation, the beam path included a TD 488/552/638 beam-splitter. Scans were performed to obtain 10–15 optical Z sections of 2mm

each with a dry Leica 20× objective (numerical aperture 0.70, working distance 0.5 mm), using LAS X software (Leica Application Suite X 3.1.1.15751).

Behavioral apparatus for head-fixed imaging—The behavioral apparatus consisted of 2m long, 7.5 cm wide cotton fabric belt stretched between 15 cm diam. laser-cut plastic wheels, mounted on an aluminum frame (8020.net). Task events were controlled through a custom software (*Be-Mate* algorithm implemented in Java)[82] on the PC that would send and receive instructions from serial communication with a microcontroller (Arduino DUE) and an associated printed circuit board (OpenMaze OM4 PCB) on the behavior apparatus, which managed the water delivery system, lick port sensor and synchronization with the imaging system, as well as the position tracking circuit. The axle of the treadmill wheel was attached to a quadrature rotary encoder (US Digital #MA3-A10-125-B) connected to a custom quadrature decoder board and Arduino Nano (courtesy of Wen Li). Angular displacement was converted into a virtual linear distance based on the circumference of the treadmill wheels, and laps were determined by reading an RFID chip on the treadmill belt attachment point with an RFID reader (Sparkfun #ID12LA) mounted under the animal's head fixation point. A water reservoir connected to a water delivery port consisting of a small gavage needle (Cadence Science) was placed within reach of the mouse's tongue. A capacitance touch sensor (Sparkfun MPR121) was attached to the water port to measure licking and the sensor was connected to the Arduino/OM4 PCB. Small 2–3ml drops of water were delivered by the brief opening a solenoid valve (Parker Hannefin) connected to the water port. Rewards were triggered at locations each lap when mice entered a 10cm long reward zone on the track and were available in response to tongue contact with a capacitive sensor, until mice exited the reward zone or 3 sec had elapsed, making the reward delivery operant. Mice were monitored using an IR camera (PS3eye) and illuminated using an IR LED array.

Habituation and behavioral tasks during head-fixed imaging—After a minimum of 1 week recovery period, mice underwent a water restriction scheme (>85% pre-deprivation weight), habituated to handling and trained to run on treadmill while head-restrained. Mice initially received 20 randomly placed rewards per lap, and the reward frequency was decreased until the mice ran reliably for 3 randomly placed rewards per lap at a rate of at least 1 lap per min. The training period typically lasted a week (2 training sessions/day, 15 min each) until the mice were able to run for at least 1 lap/ minute and seek reward from one of 3 reward zones that were randomly selected along the belt on each traversal by licking the water delivery port. Randomization of reward zones during training encouraged mice to continuously run and lick simultaneously. We discarded mice that did not perform sufficiently to receive getting all their daily water supply during treadmill training, and were not motivated to move on the treadmill. During the training period mice ran on a cue-less 'burlap' belt and progressed to a different belt containing cues of different modalities and different reward delivery schemes as described below. Mice were imaged for three or two consecutive sessions/day, each 15 minutes long, for the duration of 7–10 days. In all experiments, the treadmill belt material was changed between sessions to reduce the chances of urine contamination which might act as an additional olfactory cue. In between experiments, belts were washed with Tergazyme (Alconox).

Context switching paradigm: For context-switch experiments, mice ran at will through cue rich belts, previously unseen prior to the start of imaging experiments to receive 3 randomly placed 'hidden' water rewards. Similar to our previous work[9], Context A and B consisted of the same treadmill belt (the same sequence of three joined fabric ribbons) but was distinct in its visual, auditory, tactile, and olfactory stimuli (see Figure S3G,J). To allow for comparison of GC activity between similar contexts, the same three fabrics were used in the same order, but the locations of all the tactile cues were shuffled between the two belts. For X-irradiation experiments (Figures 1, S1, 3A–C, S3A–B,G–I) olfactory cue was delivered ambiently by placing inside the rig a 1ml tube containing a small corner of a filter paper submerged in 100ml undiluted isoamyl acetate (banana odor, Sigma W205532) or menthalactone (mint odor, Sigma W376418) , while for silecing experiments (Figures 2, S2, 3A–C, S3C–F, J–N), undiluted isoamyl acetate or menthalactone were added to syringe filters (Whatman #6888–2527) and delivered by opening a solenoid valve (SMC) connected to a flow controller delivering constant airflow of compressed medical grade air for 1s (~3psi). Within this task, we defined cue encoding mGCs as those with peak Ca^{2+} event rate within the boundaries of the cues (10 cm wide for tactile and 20cm for odor). Place encoding mGCs were defined as those with peak Ca^{2+} event rate outside of the boundary of the cues on the treadmill belt during the second exposure to context A (A'), and selected cross-registered neurons in Context A (first exposure) or B. For selection of putative cue and place cells in the contexts in X-IR experiments, see Figure S3G for the location of cues in blue dashed rectangles and areas on the belt without discrete tactile cues, in orange straight lines. For hM4Di silencing experiments, see Figure S3J for the location of tactile cues, odor cue location in blue dashed rectangles and areas on the belt without discrete cues in orange straight lines.

Cue manipulation paradigm: For cue manipulation experiments mice ran on a motorized belt to lick for randomly placed rewards as described previously[39]. For motorized running (Figures 4–5), a 12V DC gear motor was attached to the axle of the treadmill connected to a separate Arduino/OpenMaze shield using pulse-width modulation to adjust the rotation speed. For naïve mice, we initiated the motorized belt after mice were able to run for at least 1 lap/ minute and for mice that completed the context or GOL task we adjusted the speed to the natural velocity of each mouse and proceeded training on the motor on a burlap training belt for 1–2 more days. Olfactory stimuli consisted of undiluted isoamyl acetate (IAA, Sigma W205532) which was added to syringe filters (Whatman #6888–2527) and delivered at indicated locations on different laps by opening a solenoid valve (SMC) connected to a flow controller delivering constant airflow of compressed medical grade air for 1s (~3psi). To isolate cue-selective responses among the granule cell population, normal cue laps in which the olfactory, cue was presented in the middle of the treadmill track (90–110cm) were interspersed with occasional laps (10–20% of laps) in which the same cue was omitted ("omit" laps), or shifted forward ¼ of the track ("shift" laps, 40–60cm cue position). Among all of the spatially tuned neurons, "odor cue cells" were defined as those with averaged spatial fields that overlapped with at least 50% of the 45th and 55th bins and had peak amplitude at least two times larger than those in cue-omitted laps. "Lap-cue cells" were defined as those with averaged spatial fields overlapping at least 50% of the region wrapping around the 90th and 10th bins in the normal laps and have peak amplitude in cue-omitted

laps and cue shifted laps not exceeding than at least two times of that in normal laps. The remaining cells constituted the “place cells”.

Goal oriented learning (GOL) paradigm: After completing the context switching paradigm in which mice ran for 3 random rewards, the animals were trained to search for a single, fixed reward-location on a cue-less burlap belt for 1 day before beginning the goal-oriented learning task (a 15 min. session, location different from that in the GOL task). For GOL task (Figure 6, S5), the belt consisted of a tactile cue in the lap boundary (a 10 cm wide velcro band) and another tactile cue in the middle of the belt (a 10 cm wide soft circular material). The rewarded zone was chosen to lie in a cue-poor region of the belt to avoid direct cue–reward pairings. In the first two ‘training’ sessions, animals ran to search for a hidden spatially restricted (one 20cm zone) operantly delivered water reward following the middle cue at the 90–110cm position. In the ‘reversal’ session, the reward zone was moved to a new location (40–60cm position), while the other features of the belt and context were kept the same as in the training sessions. We used the lick rates to measure performance on the goal-directed task by calculating the number of licks normalized to the occupancy at each bin. We considered anticipatory window as the 20cm zone before the rewards were available and reward/goal window as the 20 cm zone within the reward delivery area.

In vivo two-photon imaging—Imaging was conducted using a microscope setup which consists of 8kHz resonant galvanometer (*Bruker*) mounted to a mirror-based multi-photon microscopy system (*Prairie Technologies*) and an ultra-fast pulsed laser beam (920-nm wavelength; *Chameleon Ultra II, Coherent*, 20–40-mW average power at the back focal plane of the objective) controlled with an electro-optical modulator (*Conoptics*, Model 302 RM). GCaMP fluorescence was excited through a 40x water immersion objective (Nikon NIR Apo, 0.8 NA, 3.5 mm WD) and fluorescence signals detected with photomultiplier tubes (*Hamamatsu 7422P-40*), acquired with PrairieView software (*Prairie*) at 30fps frame rate (512×512 pixels, 1.3 mm/pixel). A custom dual stage preamp (1.4×10^5 dB, Bruker) was used to amplify signals prior to digitization. Two goniometers (Edmund Optics) were used to adjust the angle of each mouse’s head in order to achieve the same imaging plane over multiple sessions.

Pre-processing for Ca^{2+} imaging: Movies were motion corrected using NoRMCorre algorithm using a non-rigid registration method that splits the field of view (FOV) into overlapping patched that are registered separately then merged by smooth interpolation[90]. Videos were then spatially and temporally down-sampled by 2 to reduce noise and the computational power required for cell segmentation. Spatial and temporal components for individual cells were extracted using the singular value decomposition method by *Suite2p* algorithm (https://github.com/cortex-lab/Suite2P), followed by visual inspection of the regions of interest (ROIs) using the Suite2p graphical user interface.

We selected only the clearly identifiable granule cells using the Suite2p GUI algorithm which was aided by the easy differentiation of the granule cell layer due to the clear laminar structure of the DG, as well as the distinctly small round shape of the granule cells compared to large cell bodies of interneurons or mossy cells (see Figure S1B for representative FOVs),

yet we cannot exclude the possibility that a small fraction of the cells are not mGCs. To obtain total number of DG granule cells within the imaging fields of view in a subset of total sessions, time averaged images were segmented and counted using the *Cellpose* algorithm (https://github.com/MouseLand/cellpose) followed by manual inspection to discard large cell bodies corresponding to mossy cells or other hilar interneurons from analysis.

Transient detection: Ca^{2+} transients were detected and used for all subsequent analysis. Suite2p extracted calcium traces (C) were smoothed with a 1 second boxcar filter. dF was subsequently calculated as the 1st order derivative of the smoothed signals. For each cell in each session a transient detection threshold was calculated as 4 standard deviations above the mean of the smoothed dF vector. Transients were detected from the of the smoothed dF vectors as the time-points corresponding to the largest amplitude peak within above-threshold segments lasting at least 3 seconds. If two or more such transient peaks were detected within 3 seconds of each other, only the largest amplitude one was kept. Since transients can bias the threshold estimates, a new baseline was calculated after removing the 3 seconds before and 2 seconds after each transient peak and the transients were re-calculated as above, using this new baseline threshold. This re-baselining procedure was iteratively repeated a total of two times following the initial transient detection. We did not detect any differences in baseline stability (standard deviation of dF Ca^{2+} signal) between experimental groups (data not shown).

Behavioral and Calcium Data Alignment: Behavioral data was aligned to Ca^{2+} data using the record of a synchronization signal between the two computers used for data collection. Behavioral data was down-sampled to match Ca^{2+} imaging data.

Quantification and statistical analysis

Data were analyzed using custom-written routines implemented in MATLAB. Plots were generated in MATLAB and Prism.

Identification of spatially-tuned neurons: We restricted our analysis to continuous running at least 2 sec in duration and with a minimum peak speed of 5 cm/sec. For each lap crossing, position data and Ca^{2+} transient events for each cell were binned into 2 cm-wide windows (100 bins), generating raw vectors for occupancy-by-position and calcium transient numbers-by-position which were then circularly smoothed with a Gaussian kernel (SD = 5 cm). A firing rate-by-position vector was computed by dividing the smoothed transient number vector by the smoothed occupancy vector. Within each lap, we circularly shuffled the positions 1000 times and recomputed firing rate-by-position vectors to generate a null distribution for each spatial bin. A spatially selective cell was defined that met the following criteria: (a) the cell should fire above its mean firing rate within its spatial field in at least 20% of laps or for a minimum of 3 laps; and (b) observed firing should be above 99% of the shuffled distribution for at least 5 consecutive spatial bins (10 cm) wrapping around the two edges of the belt. For cue manipulation experiments, we have identified spatially tuned neurons by excluding bins in which sensory cues were omitted or shifted and calculated firing rate vectors in these laps separately. For context discrimination experiments, among all the spatially tuned cells, cue cells were defined as those with peak spatial field rate that was

within 15th and 20th bins, 50th and 55th bins, 80th and 85th bins corresponding to the tactile cues (or the odor cue which was delivered within 50th and 55th bins for CNO experiments). The remaining cells constituted the 'place cells'. For cue manipulation experiments, *"middle cue cells"* (also termed as odor-cue) were defined as those with peak amplitude that was within 50th and 55th bins and were at least two times larger than those in cue-omitted laps in the same session. These experiments also had "lap-cue cells" due to prominent texture of the edges of the belt and were defined as those with averaged spatial fields overlapping at least 50% of the region wrapping around the 90th and 10th bins in the normal laps that were treated separately. The remaining cells constituted the 'place cells'.

Spatial information, stability, consistency, and emergence of spatial fields: To calculate a measure for spatial information content for granule cells we adapted a traditional method of spatial information assessment[9,44,53] to Ca^{2+} imaging data. For each cell, we used the firing rate-by-position vector and shuffled null distribution computed above and calculated the spatial information content as follows:

$$\mathrm{SPE} = \sum_i p_i \frac{\lambda_i}{\lambda} \log_2 \frac{\lambda_i}{\lambda}$$

Where λ is the overall mean event rate, λ_i is the mean event rate of each cell in the i^{th} bin, p_i is the probability of that mouse being in the i^{th} bin that is occupancy in the i^{th} bin/ 15mins.

To account for the fact that low firing rates artificially produce high spatial information scores, we subtracted the mean of the shuffled information per spike from observed information per spike, divided by the standard deviation of the shuffled values to determine the spatial variance for each cell. Therefore, the amount of spatial information is inferred from differences in normalized Ca^{2+} activity in each neuron and reported as bits per seconds. The consistency of place field firing was determined as the cross-correlation between the averaged firing rate-by-position vector of the first and the second halves of the total number of cue normal laps within a session. We determined place field onset lap in cue normal laps as described previously[91]. Briefly, starting on lap 1 we searched for a significant Ca^{2+} transient event present within the boundaries of the previously determined mean spatial field calculated from all the laps in the session. If one were found we would then search for Ca^{2+} transient event on each of the next 4 laps. If 3 of the 5 laps had Ca^{2+} transients within the mean place field boundaries, lap 1 would be considered the place field onset lap. If either lap 1 had no Ca^{2+} transient or less than 3 of the 5 laps had Ca^{2+} transient, we would move to lap 2 and repeat the search.

Multi-Session Cell Tracking: Cells were tracked across sessions using CellReg algorithm reported in[42]. Briefly, rigid alignment with both translations and rotations was performed on spatial footprint projections of each session and manually inspected for quality. To improve performance with our data, we modified the CellReg source code to consider complete spatial footprints instead of centroids during alignment. The centroid distance between neighbors was then calculated and used to create a probabilistic model that estimated the expected error rate at different thresholds. The optimal centroid distance

threshold was chosen by the algorithm and used to match cells. A clustering algorithm then refined these decisions previously made using pairwise comparisons.

Following cell registration, tracked cells were matched with their corresponding functional cell types (i.e. Spatially tuned cell, non-spatially tuned cell for Figure S3B,D or mid-cue, place cells for Figure S3H,I,K,L 5D, as described above). The analyses presented in Figures S3 and 5 are carried out in pairwise sessions, to maximize the number of cells in each comparison and to minimize the total number of comparisons. For context comparisons we used Context A' and for multiday comparisons we used Day1 as the reference sessions. To calculate the fraction of cells that maintain their identity, cell pairs that were counted as being the same cell type in both sessions was divided by all of that cell type in the reference session. In order to derive a null distribution for preservation of pairwise identity, we randomly permutated the cell IDs of all the tracked cells in pairwise sessions 1000 times and calculated the fraction of cells that were the same, among all of that cell type in the normal session. We calculated p-values by comparing actual data to this null distribution, 97.5^{th}% of the null distribution is presented dotted lines in Figure S3 B,D.

Rate correlation, population vector (PV) and remapping index analysis: Comparison of single cell activity between different sessions was calculated using Pearson's correlation of the spatially binned, averaged firing rate-by-position vector in different context sessions in Figure S1, different lap types in Figures 4 and 5. The variability in neural population activity between different contexts (Figure S1) was calculated by using Pearson's correlation on each 2 cm bins of the firing rate-by-position vector along the treadmill. In Figure 3 and S3, remapping index was calculated by subtracting the mean averaged correlation between different contexts (Contexts AB and A'B) from the correlation between similar contexts (sequential exposures to Context A, Contexts AA'). Granule cells' averaged Ca^{2+} rates are plotted against their remapping index in control and X-IR mice within a sliding 25 percentile-wide window of their averaged rates in Ctx A-A'-B. GCs' CNO induced normalized rate differences plotted against their remapping index in $Di^{F/F}$ and $Ascl^{CreER}Di^{F/F}$ mice using a sliding 25 percentile-wide window averages of the differences. Figure 4 and 5, spatial firing rates for each spatially tuned cell on normal middle cue laps were cross-correlated with firing rates on shift or omit laps on each 2 cm bins of the firing rate-by-position vector along the treadmill in order to visualize the cross-correlation peak offset (i.e. rate remapping) after cue manipulation. Temporal rate modulation of cue cells was calculated as the ratio of peak rate during cue shifted laps relative to the more frequent middle cue laps for all cue cells on days 1, 1' and 7.

Cross-Session Bayesian Reconstruction Analysis: To calculate the probability of the animal's position given a short time window of neural activity, we used a previously published method based on Bayesian reconstruction algorithm (Davidson, Wilson 2009, Grosmark and Buzsáki, 2016). We selected cells that were cross-registered in all three sessions, regardless of their spatial tuning. For Figure 1,2 and S2, we generated a template based on the activity of cells in the second session (Context A'), and tested the position estimate in the first or the third session (Context A and B). For figure 5, template session was Day 1, testing sessions were Day 1' and Day7.

Bayesian reconstruction of virtual position was performed utilizing a template comprising of all cell's smoothed transient rate-by-position vectors as:

$$Pr(pos \mid spikes) = \left(\prod_{i=1}^{n} f_i(pos)^{sp_i}\right) e^{-\tau \sum_{i=1}^{n} f_i(pos)}$$

Where $f_i(pos)$ is the value of the transient rate-by-position vector of the i^{th} cell at position pos, sp^i is the number of transients fired by the i^{th} place cell in the time bin being decoded, τ is the duration of the time bin and n is the total number of place cells. One second time bins (τ) were used for Bayesian reconstruction and only bins with non-zero transient rates were used for Bayesian decoding. Posterior probabilities were subsequently normalized to one:

$$Pr(pos \mid spikes) = \frac{Pr(pos \mid spikes)}{\sum_{i=1}^{P_n} Pr(pos_i \mid spikes)}$$

Where P_n is the total number of positions (2 cm bins). When assessing reconstruction accuracy, the position corresponding to the maximal posterior probability was taken. In sessions with multiple lap types (Figure 5), post-reconstruction, we divided the time bins by lap types (for instance, by 'omit' or 'shift' laps). To determine the decoding error, we calculated the absolute difference between the animal's actual position and the maximum posterior probability in that bin. A given session's decoding error was defined as the median absolute error across time bins in that session. In order to calculate the decoding discrimination index we subtracted the decoder error calculated by subtracting Context A from that of Context B and dividing by the sum of these values ($\text{Error}_{\text{Different Context}} - \text{Error}_{\text{Same Context}}$)/($\text{Error}_{\text{Different Context}} + \text{Error}_{\text{Same Context}}$). To determine the stability index, we subtracted the decoder error of Day7 from that of Day1' and divided by the sum of these values ($\text{Error}_{\text{D1}} - \text{Error}_{\text{D7}}$)/ ($\text{Error}_{\text{D1}} + \text{Error D7}$).

Statistics

Differences between experimental groups were determined using mixed design repeated measures two-way ANOVA and Bonferroni's multiple comparisons test. Means were compared by Wilcoxon rank sum test (matched samples) or Mann-Whitney test (unpaired samples). Differences in the distributions from different experimental groups were calculated using two-sample Kolmogorov-Smirnov test. Linear regression analyses with Pearson's correlation coefficient were calculated for correlations of remapping index and mGC activity (Figure 3) or activity correlation between sessions and anticipatory lick rate (Figure 6) followed by Fisher's Z test to measure differences between experimental groups. ANOVA statistics were calculated using Prism software, all other statistics were calculated using MATLAB.

Supplementary Material

Refer to Web version on PubMed Central for supplementary material.

Acknowledgements

This work was funded by NIH K99 MH12226 to S.N.T., Revson Fellowship in Biomedical Science to A.D.G., K01 AG054765 to V.M.L.; R37 MH068542, R01 MH083862 to R.H., the Hope for Depression Research Foundation (HDRF RGA-13-003) to R.H., NYSTEM (C029157) to R.H., NIMH R01 MH100631, NINDS R01NS094668, and NINDS U19NS104590 to A.L., RF1 AG080818 to RH and AL.

References

1. Ge S, Yang C-H, Hsu K-S, Ming G-L, and Song H (2007). A critical period for enhanced synaptic plasticity in newly generated neurons of the adult brain. Neuron 54, 559–566. 10.1016/j.neuron.2007.05.002. [PubMed: 17521569]
2. Marín-Burgin A, Mongiat LA, Pardi MB, and Schinder AF (2012). Unique processing during a period of high excitation/inhibition balance in adult-born neurons. Science 335, 1238–1242. 10.1126/science.1214956. [PubMed: 22282476]
3. Schmidt-Hieber C, Jonas P, and Bischofberger J (2004). Enhanced synaptic plasticity in newly generated granule cells of the adult hippocampus. Nature 429, 184–187. 10.1038/nature02553. [PubMed: 15107864]
4. Snyder JS, Kee N, and Wojtowicz JM (2001). Effects of adult neurogenesis on synaptic plasticity in the rat dentate gyrus. J. Neurophysiol 85, 2423–2431. 10.1152/jn.2001.85.6.2423. [PubMed: 11387388]
5. Sahay A, Scobie KN, Hill AS, O'Carroll CM, Kheirbek MA, Burghardt NS, Fenton AA, Dranovsky A, and Hen R (2011). Increasing adult hippocampal neurogenesis is sufficient to improve pattern separation. Nature 472, 466–470. 10.1038/nature09817. [PubMed: 21460835]
6. Denny CA, Burghardt NS, Schachter DM, Hen R, and Drew MR (2012). 4- to 6-week-old adult-born hippocampal neurons influence novelty-evoked exploration and contextual fear conditioning. Hippocampus 22, 1188–1201. 10.1002/hipo.20964. [PubMed: 21739523]
7. Gu Y, Arruda-Carvalho M, Wang J, Janoschka SR, Josselyn SA, Frankland PW, and Ge S (2012). Optical controlling reveals time-dependent roles for adult-born dentate granule cells. Nat. Neurosci 15, 1700–1706. 10.1038/nn.3260. [PubMed: 23143513]
8. Nakashiba T, Cushman JD, Pelkey KA, Renaudineau S, Buhl DL, McHugh TJ, Rodriguez Barrera V, Chittajallu R, Iwamoto KS, McBain CJ, et al. (2012). Young dentate granule cells mediate pattern separation, whereas old granule cells facilitate pattern completion. Cell 149, 188–201. 10.1016/j.cell.2012.01.046. [PubMed: 22365813]
9. Danielson NB, Kaifosh P, Zaremba JD, Lovett-Barron M, Tsai J, Denny CA, Balough EM, Goldberg AR, Drew LJ, Hen R, et al. (2016). Distinct Contribution of Adult-Born Hippocampal Granule Cells to Context Encoding. Neuron 90, 101–112. 10.1016/j.neuron.2016.02.019. [PubMed: 26971949]
10. Huckleberry KA, Shue F, Copeland T, Chitwood RA, Yin W, and Drew MR (2018). Dorsal and ventral hippocampal adult-born neurons contribute to context fear memory. Neuropsychopharmacol. Off. Publ. Am. Coll. Neuropsychopharmacol 43, 2487–2496. 10.1038/s41386-018-0109-6.
11. Lissek S, Rabin S, Heller RE, Lukenbaugh D, Geraci M, Pine DS, and Grillon C (2010). Overgeneralization of conditioned fear as a pathogenic marker of panic disorder. Am. J. Psychiatry 167, 47–55. 10.1176/appi.ajp.2009.09030410. [PubMed: 19917595]
12. Yassa MA, Mattfeld AT, Stark SM, and Stark CEL (2011). Age-related memory deficits linked to circuit-specific disruptions in the hippocampus. Proc. Natl. Acad. Sci 108, 8873–8878. 10.1073/pnas.1101567108. [PubMed: 21555581]
13. Shelton DJ, and Kirwan CB (2013). A possible negative influence of depression on the ability to overcome memory interference. Behav. Brain Res 256, 20–26. 10.1016/j.bbr.2013.08.016. [PubMed: 23948219]
14. Lange I, Goossens L, Michielse S, Bakker J, Lissek S, Papalini S, Verhagen S, Leibold N, Marcelis M, Wichers M, et al. (2017). Behavioral pattern separation and its link to the neural mechanisms of fear generalization. Soc. Cogn. Affect. Neurosci 12, 1720–1729. 10.1093/scan/nsx104. [PubMed: 29036532]

15. Boldrini M, Galfalvy H, Dwork AJ, Rosoklija GB, Trencevska-Ivanovska I, Pavlovski G, Hen R, Arango V, and Mann JJ (2019). Resilience Is Associated With Larger Dentate Gyrus, While Suicide Decedents With Major Depressive Disorder Have Fewer Granule Neurons. Biol. Psychiatry 85, 850–862. 10.1016/j.biopsych.2018.12.022. [PubMed: 30819514]
16. Yassa MA, and Stark CEL (2011). Pattern separation in the hippocampus. Trends Neurosci. 34, 515–525. 10.1016/j.tins.2011.06.006. [PubMed: 21788086]
17. Kheirbek MA, Klemenhagen KC, Sahay A, and Hen R (2012). Neurogenesis and generalization: a new approach to stratify and treat anxiety disorders. Nat. Neurosci 15, 1613–1620. 10.1038/nn.3262. [PubMed: 23187693]
18. Lacefield CO, Itskov V, Reardon T, Hen R, and Gordon JA (2012). Effects of adult-generated granule cells on coordinated network activity in the dentate gyrus. Hippocampus 22, 106–116. 10.1002/hipo.20860. [PubMed: 20882540]
19. Ikrar T, Guo N, He K, Besnard A, Levinson S, Hill A, Lee H-K, Hen R, Xu X, and Sahay A (2013). Adult neurogenesis modifies excitability of the dentate gyrus. Front. Neural Circuits 7, 204. 10.3389/fncir.2013.00204. [PubMed: 24421758]
20. Drew LJ, Kheirbek MA, Luna VM, Denny CA, Cloidt MA, Wu MV, Jain S, Scharfman HE, and Hen R (2016). Activation of local inhibitory circuits in the dentate gyrus by adult-born neurons. Hippocampus 26, 763–778. 10.1002/hipo.22557. [PubMed: 26662922]
21. Anacker C, Luna VM, Stevens GS, Millette A, Shores R, Jimenez JC, Chen B, and Hen R (2018). Hippocampal neurogenesis confers stress resilience by inhibiting the ventral dentate gyrus. Nature 559, 98–02. 10.1038/s41586-018-0262-4. [PubMed: 29950730]
22. McHugh SB, Lopes-dos-Santos V, Gava GP, Hartwich K, Tam SKE, Bannerman DM, and Dupret D (2022). Adult-born dentate granule cells promote hippocampal population sparsity. Nat. Neurosci, 1–11. 10.1038/s41593-022-01176-5. [PubMed: 34992291]
23. Luna VM, Anacker C, Burghardt NS, Khandaker H, Andreu V, Millette A, Leary P, Ravenelle R, Jimenez JC, Mastrodonato A, et al. (2019). Adult-born hippocampal neurons bidirectionally modulate entorhinal inputs into the dentate gyrus. Science 364, 578–583. 10.1126/science.aat8789. [PubMed: 31073064]
24. O'Keefe J, and Dostrovsky J (1971). The hippocampus as a spatial map. Preliminary evidence from unit activity in the freely-moving rat. Brain Res. 34, 171–175. [PubMed: 5124915]
25. Burgess N, and O'Keefe J (1996). Neuronal computations underlying the firing of place cells and their role in navigation. Hippocampus 6, 749–762. 10.1002/(SICI)1098-1063(1996)6:6<749::AID-HIPO16>3.0.CO;2–0. [PubMed: 9034860]
26. Latuske P, Kornienko O, Kohler L, and Allen K (2017). Hippocampal Remapping and Its Entorhinal Origin. Front. Behav. Neurosci 11, 253. 10.3389/fnbeh.2017.00253. [PubMed: 29354038]
27. Kubie JL, Levy ERJ, and Fenton AA (2020). Is hippocampal remapping the physiological basis for context? Hippocampus 30, 851–864. 10.1002/hipo.23160. [PubMed: 31571314]
28. Colgin LL, Moser EI, and Moser M-B (2008). Understanding memory through hippocampal remapping. Trends Neurosci. 31, 469–477. 10.1016/j.tins.2008.06.008. [PubMed: 18687478]
29. Marr D (1971). Simple memory: a theory for archicortex. Philos. Trans. R. Soc. Lond. B. Biol. Sci 262, 23–81. 10.1098/rstb.1971.0078. [PubMed: 4399412]
30. Knierim JJ, and Neunuebel JP (2016). Tracking the flow of hippocampal computation: Pattern separation, pattern completion, and attractor dynamics. Neurobiol. Learn. Mem 129, 38–49. 10.1016/j.nlm.2015.10.008. [PubMed: 26514299]
31. Diamantaki M, Frey M, Berens P, Preston-Ferrer P, and Burgalossi A (2016). Sparse activity of identified dentate granule cells during spatial exploration. eLife 5. 10.7554/eLife.20252.
32. Danielson NB, Turi GF, Ladow M, Chavlis S, Petrantonakis PC, Poirazi P, and Losonczy A (2017). In Vivo Imaging of Dentate Gyrus Mossy Cells in Behaving Mice. Neuron 93, 552–559.e4. 10.1016/j.neuron.2016.12.019. [PubMed: 28132825]
33. GoodSmith D, Chen X, Wang C, Kim SH, Song H, Burgalossi A, Christian KM, and Knierim JJ (2017). Spatial Representations of Granule Cells and Mossy Cells of the Dentate Gyrus. Neuron 93, 677–690.e5. 10.1016/j.neuron.2016.12.026. [PubMed: 28132828]

34. Senzai Y, and Buzsáki G (2017). Physiological Properties and Behavioral Correlates of Hippocampal Granule Cells and Mossy Cells. Neuron 93, 691–704.e5. 10.1016/j.neuron.2016.12.011. [PubMed: 28132824]
35. Hainmueller T, and Bartos M (2018). Parallel emergence of stable and dynamic memory engrams in the hippocampus. Nature 558, 292–296. 10.1038/s41586-018-0191-2. [PubMed: 29875406]
36. Jung D, Kim S, Sariev A, Sharif F, Kim D, and Royer S (2019). Dentate granule and mossy cells exhibit distinct spatiotemporal responses to local change in a one-dimensional landscape of visual-tactile cues. Sci. Rep 9, 9545. 10.1038/s41598-019-45983-6. [PubMed: 31267019]
37. Woods NI, Stefanini F, Apodaca-Montano DL, Tan IMC, Biane JS, and Kheirbek MA (2020). The Dentate Gyrus Classifies Cortical Representations of Learned Stimuli. Neuron 107, 173–184.e6. 10.1016/j.neuron.2020.04.002. [PubMed: 32359400]
38. GoodSmith D, Kim SH, Puliyadi V, Ming G, Song H, Knierim JJ, and Christian KM (2022). Flexible encoding of objects and space in single cells of the dentate gyrus. Curr. Biol 32, 1088–1101.e5. 10.1016/j.cub.2022.01.023. [PubMed: 35108522]
39. Tuncdemir SN, Grosmark AD, Turi GF, Shank A, Bowler JC, Ordek G, Losonczy A, Hen R, and Lacefield CO (2022). Parallel processing of sensory cue and spatial information in the dentate gyrus. Cell Rep. 38, 110257. 10.1016/j.celrep.2021.110257. [PubMed: 35045280]
40. Santarelli L, Saxe M, Gross C, Surget A, Battaglia F, Dulawa S, Weisstaub N, Lee J, Duman R, Arancio O, et al. (2003). Requirement of Hippocampal Neurogenesis for the Behavioral Effects of Antidepressants. Science 301, 805–809. 10.1126/science.1083328. [PubMed: 12907793]
41. Burghardt NS, Park EH, Hen R, and Fenton AA (2012). Adult-born hippocampal neurons promote cognitive flexibility in mice. Hippocampus 22, 1795–1808. 10.1002/hipo.22013. [PubMed: 22431384]
42. Sheintuch L, Rubin A, Brande-Eilat N, Geva N, Sadeh N, Pinchasof O, and Ziv Y (2017). Tracking the Same Neurons across Multiple Days in Ca2+ Imaging Data. Cell Rep. 21, 1102–1115. 10.1016/j.celrep.2017.10.013. [PubMed: 29069591]
43. Zaremba JD, Diamantopoulou A, Danielson NB, Grosmark AD, Kaifosh PW, Bowler JC, Liao Z, Sparks FT, Gogos JA, and Losonczy A (2017). Impaired hippocampal place cell dynamics in a mouse model of the 22q11.2 deletion. Nat. Neurosci 20, 1612–1623. 10.1038/nn.4634. [PubMed: 28869582]
44. Grosmark AD, Sparks FT, Davis MJ, and Losonczy A (2021). Reactivation predicts the consolidation of unbiased long-term cognitive maps. Nat. Neurosci 24, 1574–1585. 10.1038/s41593-021-00920-7. [PubMed: 34663956]
45. Ray RS, Corcoran AE, Brust RD, Kim JC, Richerson GB, Nattie E, and Dymecki SM (2011). Impaired respiratory and body temperature control upon acute serotonergic neuron inhibition. Science 333, 637–642. 10.1126/science.1205295. [PubMed: 21798952]
46. Kim EJ, Ables JL, Dickel LK, Eisch AJ, and Johnson JE (2011). Ascl1 (Mash1) Defines Cells with Long-Term Neurogenic Potential in Subgranular and Subventricular Zones in Adult Mouse Brain. PLOS ONE 6, e18472. 10.1371/journal.pone.0018472. [PubMed: 21483754]
47. Yang SM, Alvarez DD, and Schinder AF (2015). Reliable Genetic Labeling of Adult-Born Dentate Granule Cells Using Ascl1 CreERT2 and Glast CreERT2 Murine Lines. J. Neurosci. Off. J. Soc. Neurosci 35, 15379–15390. 10.1523/JNEUROSCI.2345-15.2015.
48. Madisen L, Zwingman TA, Sunkin SM, Oh SW, Zariwala HA, Gu H, Ng LL, Palmiter RD, Hawrylycz MJ, Jones AR, et al. (2010). A robust and high-throughput Cre reporting and characterization system for the whole mouse brain. Nat. Neurosci 13, 133–140. 10.1038/nn.2467. [PubMed: 20023653]
49. Johnston S, Parylak SL, Kim S, Mac N, Lim C, Gallina I, Bloyd C, Newberry A, Saavedra CD, Novak O, et al. (2021). AAV ablates neurogenesis in the adult murine hippocampus. eLife 10, e59291. 10.7554/eLife.59291. [PubMed: 34259630]
50. Bergami M, Masserdotti G, Temprana SG, Motori E, Eriksson TM, Göbel J, Yang SM, Conzelmann K-K, Schinder AF, Götz M, et al. (2015). A critical period for experience-dependent remodeling of adult-born neuron connectivity. Neuron 85, 710–717. 10.1016/j.neuron.2015.01.001. [PubMed: 25661179]

51. Hill AS, Sahay A, and Hen R (2015). Increasing Adult Hippocampal Neurogenesis is Sufficient to Reduce Anxiety and Depression-Like Behaviors. Neuropsychopharmacol. Off. Publ. Am. Coll. Neuropsychopharmacol 40, 2368–2378. 10.1038/npp.2015.85.
52. Deng W, Saxe MD, Gallina IS, and Gage FH (2009). Adult-Born Hippocampal Dentate Granule Cells Undergoing Maturation Modulate Learning and Memory in the Brain. J. Neurosci 29, 13532–13542. 10.1523/JNEUROSCI.3362-09.2009. [PubMed: 19864566]
53. Skaggs WE, McNaughton BL, and Gothard KM (1993). An Information-Theoretic Approach to Deciphering the Hippocampal Code. In Advances in Neural Information Processing Systems 5, Hanson SJ, Cowan JD, and Giles CL, eds. (Morgan-Kaufmann), pp. 1030–1037.
54. Radvansky BA, Oh JY, Climer JR, and Dombeck DA (2021). Behavior determines the hippocampal spatial mapping of a multisensory environment. Cell Rep. 36, 109444. 10.1016/j.celrep.2021.109444. [PubMed: 34293330]
55. Danielson NB, Zaremba JD, Kaifosh P, Bowler J, Ladow M, and Losonczy A (2016). Sublayer-Specific Coding Dynamics during Spatial Navigation and Learning in Hippocampal Area CA1. Neuron 91, 652–665. 10.1016/j.neuron.2016.06.020. [PubMed: 27397517]
56. Sato M, Kawano M, Mizuta K, Islam T, Lee MG, and Hayashi Y (2017). Hippocampus-Dependent Goal Localization by Head-Fixed Mice in Virtual Reality. eNeuro 4. 10.1523/ENEURO.0369-16.2017.
57. Turi GF, Li W-K, Chavlis S, Pandi I, O'Hare J, Priestley JB, Grosmark AD, Liao Z, Ladow M, Zhang JF, et al. (2019). Vasoactive Intestinal Polypeptide-Expressing Interneurons in the Hippocampus Support Goal-Oriented Spatial Learning. Neuron 101, 1150–1165.e8. 10.1016/j.neuron.2019.01.009. [PubMed: 30713030]
58. Robinson NTM, Descamps LAL, Russell LE, Buchholz MO, Bicknell BA, Antonov GK, Lau JYN, Nutbrown R, Schmidt-Hieber C, and Häusser M (2020). Targeted Activation of Hippocampal Place Cells Drives Memory-Guided Spatial Behavior. Cell 183, 1586–1599.e10. 10.1016/j.cell.2020.09.061. [PubMed: 33159859]
59. Jordan JT, and Gonçalves JT (2021). Silencing of hippocampal synaptic transmission impairs spatial reward search on a head-fixed tactile treadmill task. 2021.09.03.458092. 10.1101/2021.09.03.458092.
60. Garthe A, Behr J, and Kempermann G (2009). Adult-generated hippocampal neurons allow the flexible use of spatially precise learning strategies. PloS One 4, e5464. 10.1371/journal.pone.0005464. [PubMed: 19421325]
61. Swan AA, Clutton JE, Chary PK, Cook SG, Liu GG, and Drew MR (2014). Characterization of the role of adult neurogenesis in touch-screen discrimination learning. Hippocampus 24, 1581–1591. 10.1002/hipo.22337. [PubMed: 25074617]
62. Epp JR, Silva Mera R, Köhler S, Josselyn SA, and Frankland PW (2016). Neurogenesis-mediated forgetting minimizes proactive interference. Nat. Commun 7, 10838. 10.1038/ncomms10838. [PubMed: 26917323]
63. Mathews EA, Morgenstern NA, Piatti VC, Zhao C, Jessberger S, Schinder AF, and Gage FH (2010). A Distinctive layering pattern of mouse dentate granule cells is generated by developmental and adult neurogenesis. J. Comp. Neurol 518, 4479–4490. 10.1002/cne.22489. [PubMed: 20886617]
64. Aimone JB, Deng W, and Gage FH (2011). Resolving new memories: a critical look at the dentate gyrus, adult neurogenesis, and pattern separation. Neuron 70, 589–596. 10.1016/j.neuron.2011.05.010. [PubMed: 21609818]
65. Akers KG, Martinez-Canabal A, Restivo L, Yiu AP, De Cristofaro A, Hsiang H-LL, Wheeler AL, Guskjolen A, Niibori Y, Shoji H, et al. (2014). Hippocampal neurogenesis regulates forgetting during adulthood and infancy. Science 344, 598–602. 10.1126/science.1248903. [PubMed: 24812394]
66. Frankland PW, Köhler S, and Josselyn SA (2013). Hippocampal neurogenesis and forgetting. Trends Neurosci. 36, 497–503. 10.1016/j.tins.2013.05.002. [PubMed: 23768770]
67. Sahay A, Wilson DA, and Hen R (2011). Pattern separation: a common function for new neurons in hippocampus and olfactory bulb. Neuron 70, 582–588. 10.1016/j.neuron.2011.05.012. [PubMed: 21609817]

68. Witter MP (2007). The perforant path: projections from the entorhinal cortex to the dentate gyrus. Prog. Brain Res 163, 43–61. 10.1016/S0079-6123(07)63003-9. [PubMed: 17765711]
69. Hargreaves EL, Rao G, Lee I, and Knierim JJ (2005). Major dissociation between medial and lateral entorhinal input to dorsal hippocampus. Science 308, 1792–1794. 10.1126/science.1110449. [PubMed: 15961670]
70. Knierim JJ, Neunuebel JP, and Deshmukh SS (2014). Functional correlates of the lateral and medial entorhinal cortex: objects, path integration and local-global reference frames. Philos. Trans. R. Soc. Lond. B. Biol. Sci 369, 20130369. 10.1098/rstb.2013.0369.
71. Fyhn M, Molden S, Witter MP, Moser EI, and Moser M-B (2004). Spatial representation in the entorhinal cortex. Science 305, 1258–1264. 10.1126/science.1099901. [PubMed: 15333832]
72. Miao C, Cao Q, Ito HT, Yamahachi H, Witter MP, Moser M-B, and Moser EI (2015). Hippocampal Remapping after Partial Inactivation of the Medial Entorhinal Cortex. Neuron 88, 590–603. 10.1016/j.neuron.2015.09.051. [PubMed: 26539894]
73. Rueckemann JW, DiMauro AJ, Rangel LM, Han X, Boyden ES, and Eichenbaum H (2016). Transient optogenetic inactivation of the medial entorhinal cortex biases the active population of hippocampal neurons. Hippocampus 26, 246–260. 10.1002/hipo.22519. [PubMed: 26299904]
74. Temprana SG, Mongiat LA, Yang SM, Trinchero MF, Alvarez DD, Kropff E, Giacomini D, Beltramone N, Lanuza GM, and Schinder AF (2015). Delayed coupling to feedback inhibition during a critical period for the integration of adult-born granule cells. Neuron 85, 116–130. 10.1016/j.neuron.2014.11.023. [PubMed: 25533485]
75. Lu L, Leutgeb JK, Tsao A, Henriksen EJ, Leutgeb S, Barnes CA, Witter MP, Moser M-B, and Moser EI (2013). Impaired hippocampal rate coding after lesions of the lateral entorhinal cortex. Nat. Neurosci 16, 1085–1093. 10.1038/nn.3462. [PubMed: 23852116]
76. Vivar C, Potter MC, Choi J, Lee J-Y, Stringer TP, Callaway EM, Gage FH, Suh H, and van Praag H (2012). Monosynaptic inputs to new neurons in the dentate gyrus. Nat. Commun 3, 1107. 10.1038/ncomms2101. [PubMed: 23033083]
77. Woods NI, Vaaga CE, Chatzi C, Adelson JD, Collie MF, Perederiy JV, Tovar KR, and Westbrook GL (2018). Preferential Targeting of Lateral Entorhinal Inputs onto Newly Integrated Granule Cells. J. Neurosci. Off. J. Soc. Neurosci 38, 5843–5853. 10.1523/JNEUROSCI.1737-17.2018.
78. Leal SL, Tighe SK, Jones CK, and Yassa MA (2014). Pattern separation of emotional information in hippocampal dentate and CA3. Hippocampus 24, 1146–1155. 10.1002/hipo.22298. [PubMed: 24796287]
79. O'Keefe J, and Krupic J (2021). Do hippocampal pyramidal cells respond to nonspatial stimuli? Physiol. Rev 101, 1427–1456. 10.1152/physrev.00014.2020. [PubMed: 33591856]
80. MacDonald CJ, Lepage KQ, Eden UT, and Eichenbaum H (2011). Hippocampal "time cells" bridge the gap in memory for discontiguous events. Neuron 71, 737–749. 10.1016/j.neuron.2011.07.012. [PubMed: 21867888]
81. Soltesz I, and Losonczy A (2018). CA1 pyramidal cell diversity enabling parallel information processing in the hippocampus. Nat. Neurosci 21, 484–493. 10.1038/s41593-018-0118-0. [PubMed: 29593317]
82. Bowler JC, and Losonczy A (2022). Direct Cortical Inputs to Hippocampal Area CA1 Transmit Complementary Signals for Goal-directed Navigation. 2022.11.10.516009. 10.1101/2022.11.10.516009.
83. Khatib D, Ratzon A, Sellevoll M, Barak O, Morris G, and Derdikman D (2023). Active experience, not time, determines within-day representational drift in dorsal CA1. Neuron 111, 2348–2356.e5. 10.1016/j.neuron.2023.05.014. [PubMed: 37315557]
84. Geva N, Deitch D, Rubin A, and Ziv Y (2023). Time and experience differentially affect distinct aspects of hippocampal representational drift. Neuron 111, 2357–2366.e5. 10.1016/j.neuron.2023.05.005. [PubMed: 37315556]
85. Gupta AS, van der Meer MAA, Touretzky DS, and Redish AD (2010). Hippocampal replay is not a simple function of experience. Neuron 65, 695–705. 10.1016/j.neuron.2010.01.034. [PubMed: 20223204]
86. Foster DJ (2017). Replay Comes of Age. Annu. Rev. Neurosci 40, 581–602. 10.1146/annurev-neuro-072116-031538. [PubMed: 28772098]

87. Ziv Y, Burns LD, Cocker ED, Hamel EO, Ghosh KK, Kitch LJ, Gamal AE, and Schnitzer MJ (2013). Long-term dynamics of CA1 hippocampal place codes. Nat. Neurosci 16, 264–266. 10.1038/nn.3329. [PubMed: 23396101]

88. Keinath AT, Mosser C-A, and Brandon MP (2022). The representation of context in mouse hippocampus is preserved despite neural drift. Nat. Commun 13, 2415. 10.1038/s41467-022-30198-7. [PubMed: 35504915]

89. Rechavi Y, Rubin A, Yizhar O, and Ziv Y (2022). Exercise increases information content and affects long-term stability of hippocampal place codes. Cell Rep. 41, 111695. 10.1016/j.celrep.2022.111695. [PubMed: 36417871]

90. Pnevmatikakis EA, and Giovannucci A (2017). NoRMCorre: An online algorithm for piecewise rigid motion correction of calcium imaging data. J. Neurosci. Methods 291, 83–94. 10.1016/j.jneumeth.2017.07.031. [PubMed: 28782629]

91. Sheffield MEJ, Adoff MD, and Dombeck DA (2017). Increased Prevalence of Calcium Transients across the Dendritic Arbor during Place Field Formation. Neuron 96, 490–504.e5. 10.1016/j.neuron.2017.09.029. [PubMed: 29024668]

92. Grosmark AD, and Buzsáki G (2016). Diversity in neural firing dynamics supports both rigid and learned hippocampal sequences. Science 351, 1440–1443. 10.1126/science.aad1935. [PubMed: 27013730]

Highlights:

- Mouse adult-born granule cells (abGCs) promote pattern separation.
- abGCs promote remapping of the spatial fields of place cells.
- abGCs facilitate rate remapping of sensory cue cells.
- Loss of abGCs leads to impairments in identifying new goal locations.

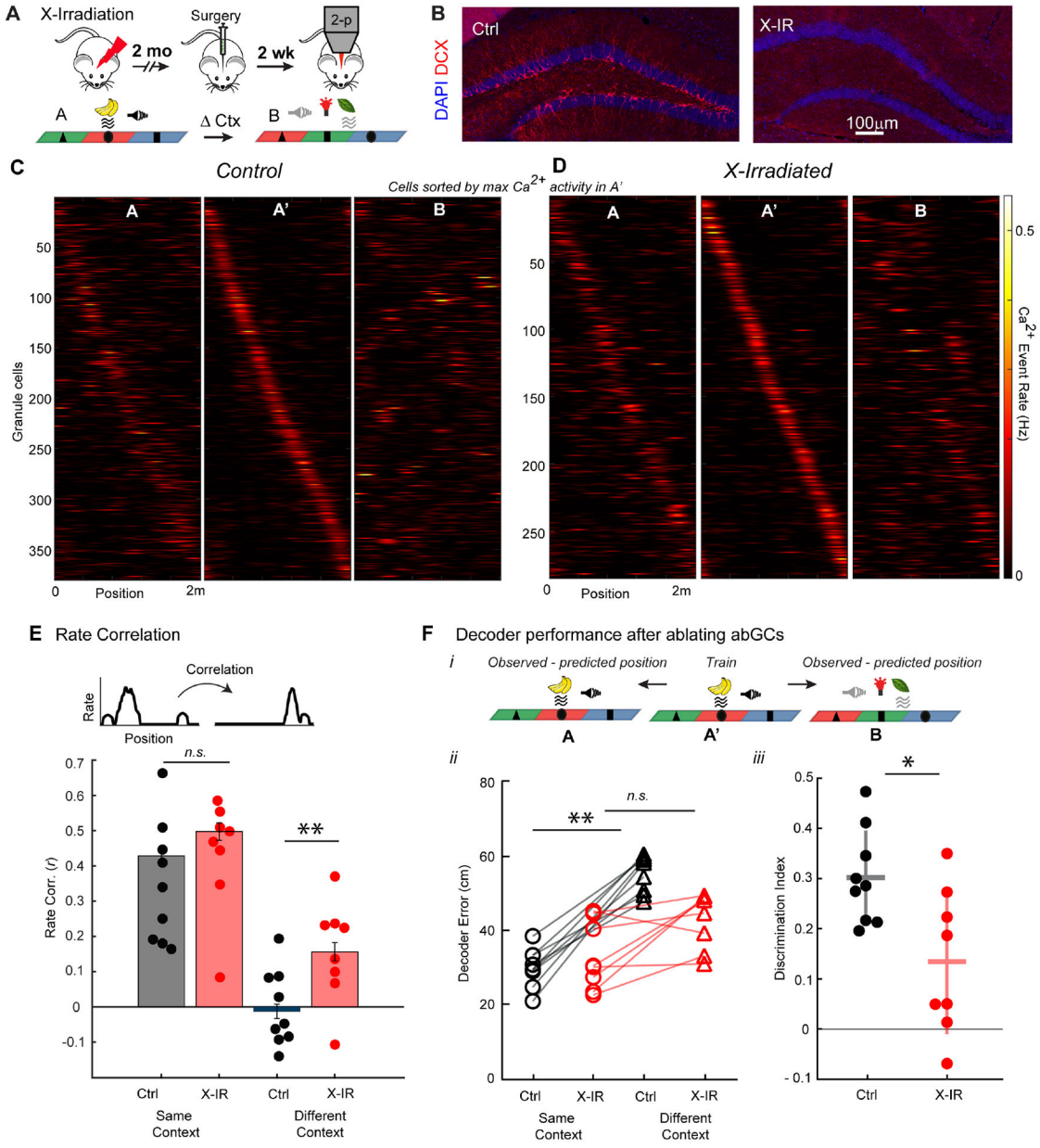

Figure 1: Chronic ablation of neurogenesis impairs context discrimination in the dentate gyrus.

A) Experimental schematic (STAR Methods).

B) Doublecortin expressing abGCs (red) in controls and X-IR mice. Blue is DAPI, scale bar = 100μm.

C) Spatial firing rate maps of GCs in control mice in contexts A-A'-B, sorted based on maximum events rate in second exposure to context A (A'). Each row across all graphs represents a single cell matched across all contexts. N_{Ctrl}=380 cells, 9 mice.

D) Spatial firing rate maps of GCs in X-IR mice, $N_{X\text{-}IR}$= 285 cells, 8 mice.

E) Top: Pearson's correlations of rate maps in the same (A-A') or different (A'-B) contexts Bottom: Bar plots: all neurons; circles: mouse. Interaction of Context vs Treatment $F_{1,15}$ = 1.379, P=0.25; Same vs Diff. Context $F_{1,15}$ = 68.98, ***P<0.0001; Ctrl vs X-IR $F_{1,15}$

= 8.510, *P=0.0106; 2-way ANOVA mixed effects model. Planned comparison for same context: $P_{Ctrl-IR}$ = 0.1955; different context: **$P_{Ctrl-IR}$ =0.0092; Bonferroni's test. **F)** ***i)*** Decoding of position in the same or different contexts from neural activity in A'. ***ii)*** Absolute median of the spatial decoder error. Control: W = 45, **$P_{Same-Different}$= 0.0039; X-IR: W = 28, $P_{Same\ Ctx-Different\ Ctx}$ = 0.0604; Wilcoxon signed rank test. ***iii)*** Discrimination index, U=13, *$P_{Ctrl-IR}$ = *0.0*274, Mann-Whitney test. Control: 97.14 ± 13.86, X-IR: 93.57 ± 9.69 GCs. Error bars, ± sem. See also Figure S1.

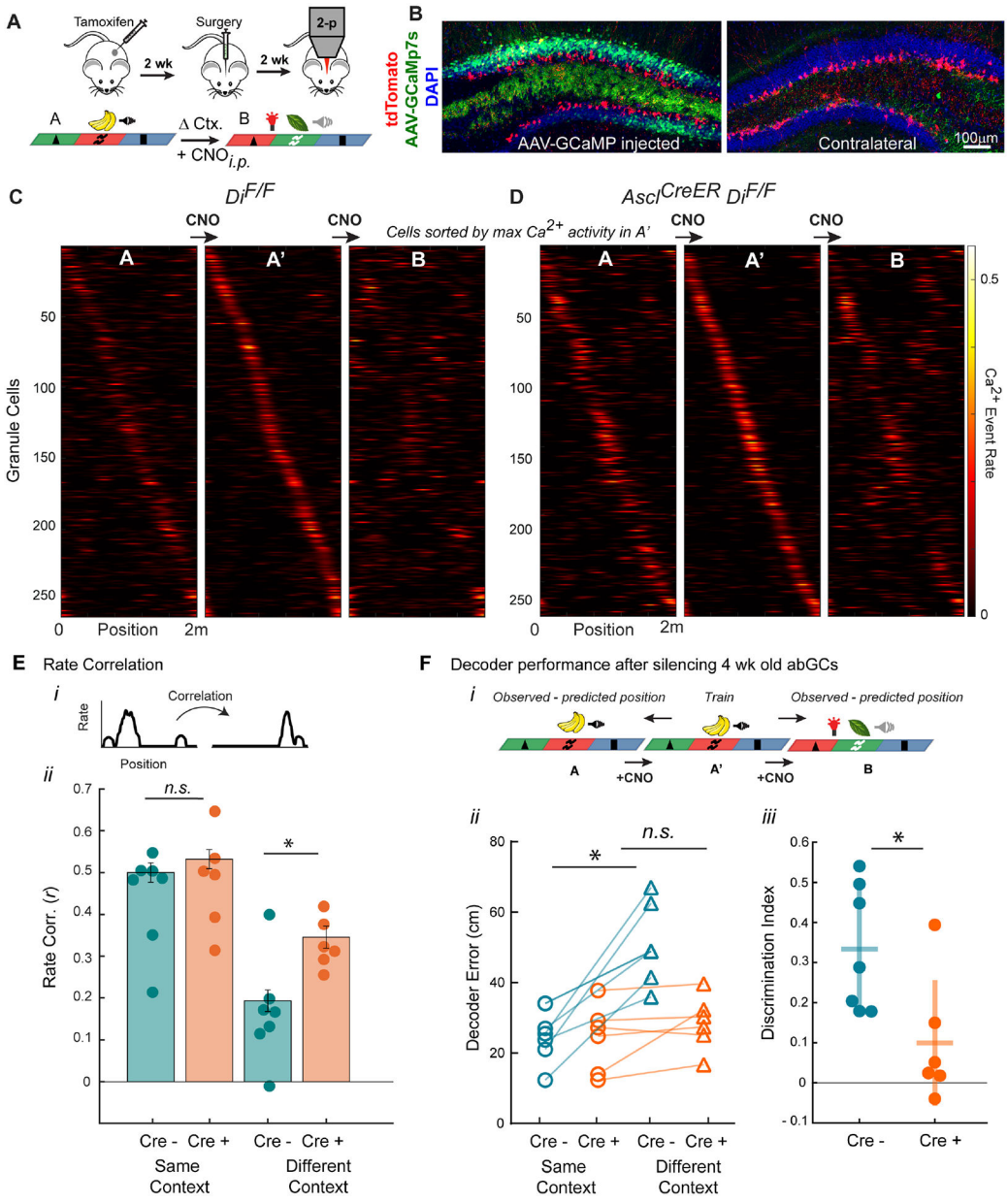

Figure 2: Acute silencing of 4-week-old adult born granule cells impairs context discrimination in the dentate gyrus

A) Experimental schematic (STAR Methods).

B) Genetically targeted abGCs (red) in the AAV injected hemisphere and contralateral hemisphere, for quantification see Figure S2B. Green is GCaMP, blue is DAPI, scale bar = 100μm.

C) Spatial firing rate maps of GCs in $Di^{F/F}$ controls in contexts A-A'-B, sorted based on maximum events rate in context A'. Each row across all graphs represents a single cell matched across all contexts. N_{Cre-}=261 cells, 7 mice.

D) Spatial firing patterns of GCs in $Ascl^{CreER}Di^{F/F}$ mice. N_{Cre+}= 275 cells, 6 mice.

E) Top: Pearson's correlations of rate maps between sequential exposures to the same (A-A') or different (A'-B) contexts. Bar plots represent group data; circles represent per

animal data. Interaction of Context vs Genotype $F_{1,11}$ = 8.34, *P=0.0145; Context $F_{1,11}$ = 113.6, ***P<0.0001; Genotype $F_{1,11}$ = 2.945, P=0.11; 2-way ANOVA mixed effects model. Planned comparison for same context: Same context: $P_{Cre- \ vs \ Cre+}$ > 0.99; Different context: *$P_{Cre- \ vs \ Cre+}$ =0.023; Bonferroni's test.

F) *i)* Decoding position in the same (A) or different (B) contexts from neural activity in A'. *ii)* Absolute median spatial decoder error. $Di^{F/F}$: W = 28, *$P_{Same- \ Different}$ = 0.0156; $Ascl^{CreER}$;$Di^{F/F}$: W = 15, $P_{Same- \ Different}$ = 0.1563; Wilcoxon signed rank test. *iii)* Discrimination index, U=4, *$P_{Cre—Cre+}$ = *0.0*140, Mann-Whitney test. $Di^{F/F}$: 83.42 ± 5.89, $Ascl^{CreER}Di^{F/F}$: 83 ± 8.68 GCs. Error bars, ± sem. See also Figure S2.

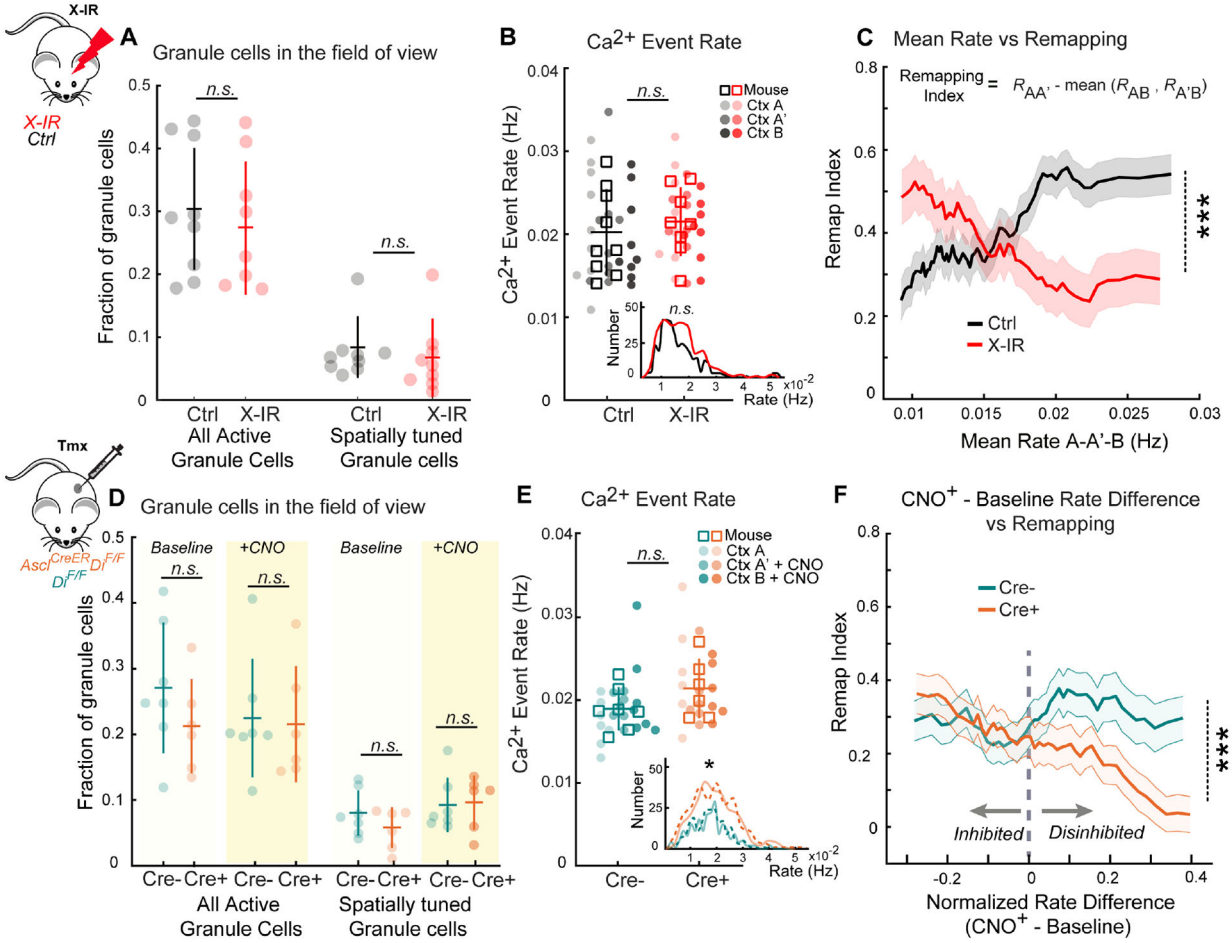

Figure 3: Adult born granule cells modulate stability of representations without changing global activity levels or spatial selectivity

A) Fraction of all active GCs and spatially tuned GCs in the imaging FOVs during context discrimination task. Active GCs: U=23, $P_{Ctrl—IR}$ = *0.23*, N_{Ctrl}= 166.22 ± 7.48, $N_{X\text{-}IR}$: 144.54 ± 6.36, spatially tuned GCs: U=26, $P_{Ctrl—IR}$ = *0.37,* N_{Ctrl}= 40.92 ± 4.36, $N_{X\text{-}IR}$: 30.04 ± 3.82, Mann-Whitney test.

B) Spatial Ca^{2+} event rates during running bouts. Squares: mouse; circles: session averages of spatial firing rates. $P_{Ctrl—IR} > 0.5$, Mann-Whitney test. Inset: Distribution of event rates of all cells averaged across all sessions, $P_{Ctrl—IR}$ =0.054, Two-sample Kolmogorov-Smirnov test.

C) GCs averaged Ca^{2+} rates vs remapping index in control and X-IR mice within a sliding 25 percentile-wide window. Pearson's R_{Ctrl}=0.1628, R_{IR}=−0.1405, ***P= *0.000340*, Fisher Z test.

D) Fraction of active GCs and spatially tuned GCs in the FOVs during context A in baseline and CNO injected sessions. Active GCs: Interaction $F_{1,11}$ = 0.49, P=0.48; CNO $F_{1,11}$ = 0.38, P=0.54; Genotype $F_{1,11}$ = 0.94, P=0.34; N-$Di^{F/F}$: 141.76 ± 7.90, N-$Ascl^{CreER}$;$Di^{F/F}$: 135.55 ± 6.35. Spatially tuned GCs: Interaction $F_{1,11}$ = 1.06, P=0.31; CNO $F_{1,11}$ = 3.43, P=0.078; Genotype $F_{1,11}$ = 0.57, P=0.45; N-$Di^{F/F}$: 45.52 ± 3.25, N-$Ascl^{CreER}$;$Di^{F/F}$: 52 ± 7.87. 2-way ANOVA mixed effects model.

E) Spatial Ca^{2+} event rates from during running bouts (squares: mouse; circles: session; darker shades: sessions with CNO injections). $P_{Cre-\ v\ Cre+} > 0.05$, Mann-Whitney test. Inset: distribution of event rates of all cells averaged across all sessions; dotted lines: baseline sessions $P_{Cre-\ v\ Cre+} = 0.018$; *straight* lines: CNO injected sessions $P_{Cre-\ v\ Cre+} = 0.016$. Two-sample Kolmogorov-Smirnov test.

F) GCs' CNO induced normalized rate differences vs. remapping index in $Di^{F/F}$ and $Ascl^{CreER}Di^{F/F}$ mice using a sliding 25 percentile-wide window averages of the differences. Pearson's R_{Cre-}=0.0241, R_{Cre+}=−0.2744, ***$P = 0.000928$, Fisher Z test. Error bars and shaded area, ± sem. See also Figure S3.

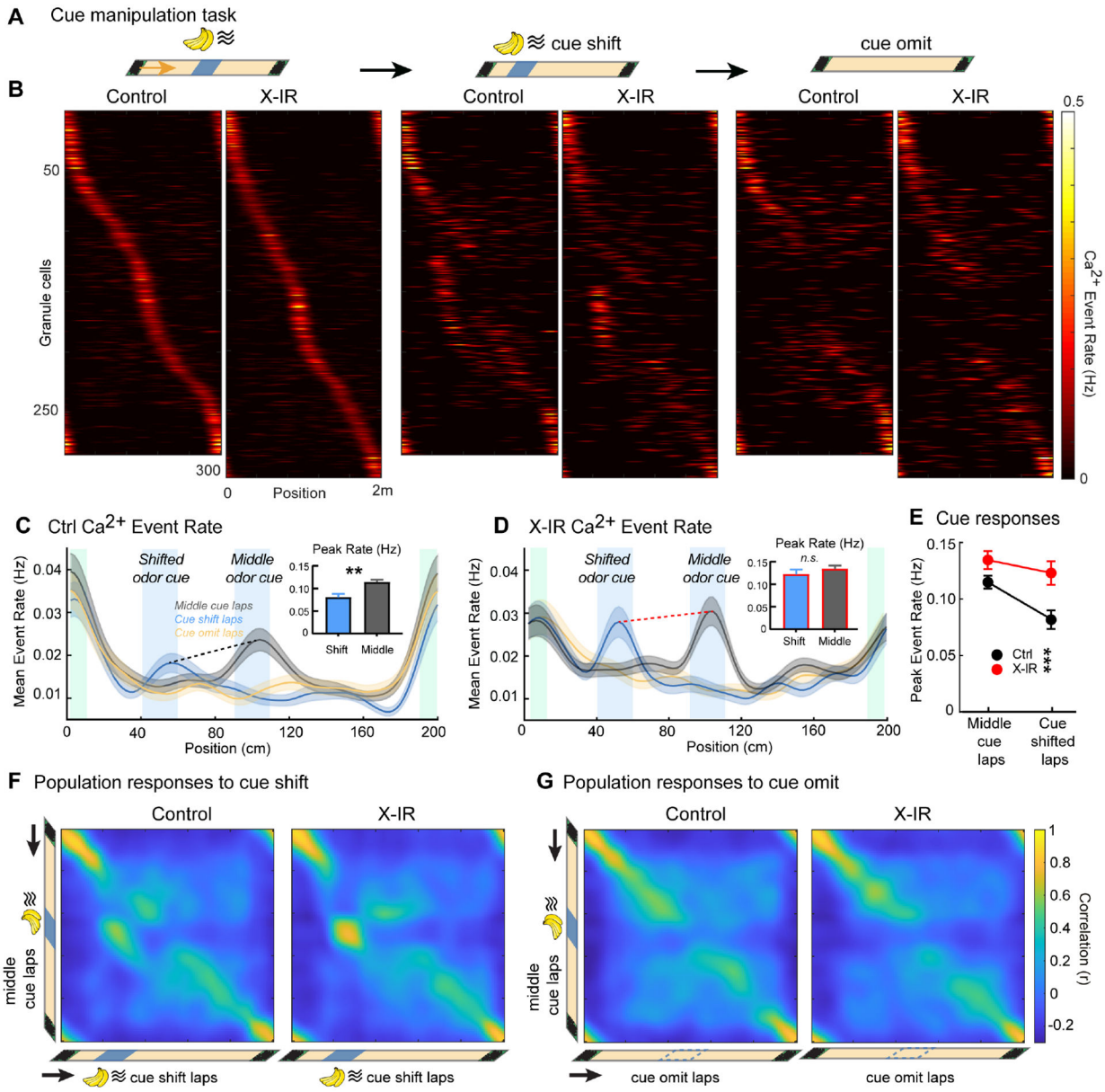

Figure 4: Chronic ablation of neurogenesis reduces rate modulation of sensory cue responses

A) Experimental schematic (top). GC activity during the spatial cue task in control and X-IR mice (bottom).

B) Lap-averaged spatial firing rates of spatially tuned neurons from controls and X-IR mice with the odor cue on normal middle location (left), cue-shifted (middle) and cue-omitted (right) laps. Each row represents activity of a single cell across lap types, sorted by activity on normal middle cue laps. N_{Ctrl}=285 cells, 8 mice; N_{IR}= 327 cells, 6 mice.

C) Average spatial firing rates by position for neurons in control mice shown in panel "B" on normal (gray), cue-shifted (blue) and cue-omitted laps (yellow). (Inset) Averaged peak firing rate (Hz) of cue cells on laps in which the cue is shifted to the 50cm location and during normal middle (100cm) cue laps. $W = -6371$, $^{**}P_{Ctrl-IR} = 0.002$.

D) Average spatial firing rates by position for neurons in X-IR mice shown in panel “B” on normal (gray), cue-shifted (blue) and cue-omitted laps (yellow). Inset as in C. $W = -6044$, $P_{Ctrl-IR} = 0.0534$, C-D, Wilcoxon signed rank test.

E) Quantification of peak firing of the cells responding to shifting of the odor cue in X-IR mice compared to controls. Interaction $F_{1,312} = 0.18$, P=0.18; Lap type $F_{1,312} = 7.307$, P=0.0072; Treatment $F_{1,312} = 13.6$, ***P=0.0003; 2-way ANOVA. Planned comparisons: Middle cue laps: $P_{Ctrl-IR} = 0.1177$; Cue shift laps: **$P_{Ctrl-IR}$ =0.0026; Tukey’s post hoc test. Control: $N_{OdorCueCells}$= 78, X-IR $N_{OdorCueCells}$= 80, Error bars, ± sem.

F) PV correlations of GCs at each treadmill position of cue-shifted (x-axis) and normal middle cue laps (y-axis) in control (left) and X-IR (right) mice.

G) PV correlations of cue-omitted laps (x-axis) and normal middle cue laps (y-axis) in control (left) and X-IR (right) mice. See also Figure S4.

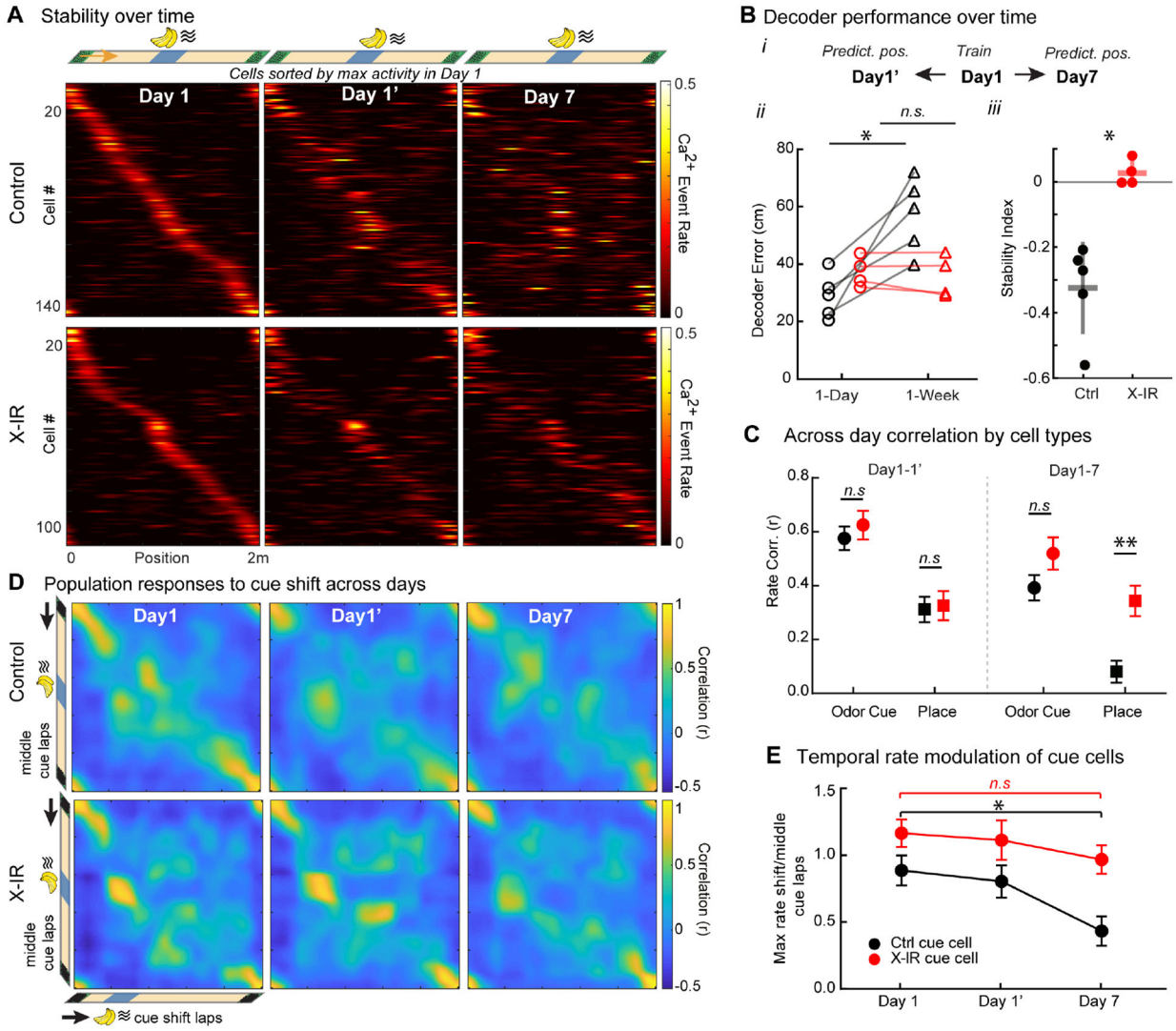

Figure 5: Chronic ablation of neurogenesis increases long-term stability of place cells and decreases rate modulation of cue cells

A) Top: Experimental schematic of imaging GC activity within a day and over one week during the spatial cue task in control and X-IR mice. Bottom: Spatial firing rates for spatially tuned neurons tracked during subsequent sessions on the same day or one week later, sorted by the peak activity on first session of Day1. N_{Ctrl}=144 cells, 5 mice; bottom, N_{IR}= 106 cells, 4 mice.

B) ***i)*** Position decoded on the same day (Day1') or one week later (Day7) from neural activity in the first session of Day 1. N_{Ctrl}= 84.4 ± 10.5; N_{IR}= 78.2 ± 7.2 GCs. ***ii)*** Absolute median spatial decoder error. W = −15, $^{*}P_{Ctrl\text{-}Day\ –\ Ctrl\text{-}Week}$ = 0.0313, W = −4, $P_{IR\text{-}Day\ –\ IR\text{-}Week}$ = 0.625, Wilcoxon signed rank test. ***iii)*** Stability index, U = 0, $^{*}P_{Ctrl\text{-}IR}$ = 0.0159, Mann-Whitney test.

C) Mean spatial firing rate correlations within the same day and 1 week later for odor-cue cells and place cells in controls and X-IR mice. Interaction $F_{3,344}$ = 2.73, $^{*}P$ = 0.043; Cell type $F_{3,344}$ = 19.37, $^{***}P$<0.001; Treatment $F_{1,344}$ = 8.82, $^{**}P$ = 0.0032; 2-way ANOVA. Day1–1': $P_{Ctrl\text{-}Cue\ –\ IR\text{-}Cue}$ = 0.99; $P_{Ctrl\text{-}Place\ –\ IR\text{-}Place}$ > 0.99; Day1–7: $P_{Ctrl\text{-}Cue\ –\ IR\text{-}Cue}$ =

0.86; ** $P_{Ctrl\text{-}Place\ –\ IR\text{-}Place}$ = 0.0016; *** $P_{Ctrl\text{-}Cue\ –\ Ctrl\text{-}Place}$ = 0.0002; $P_{IR\text{-}Cue\ –\ IR\text{-}Place}$ = 0.41; Tukey's post hoc test. $N_{Ctrl\text{-}Cue}$=39, $N_{Ctrl\text{-}Place}$=65, 5 mice, $N_{IR\text{-}Cue}$=29, $N_{IR\text{-}Place}$=47 cells, 4 mice.

D) PV correlations in controls (top) and X-IR (bottom) mice, of cue-shifted laps (x-axis) and normal middle cue laps (y-axis) for GCs that are cross-registered between days 1–1'−7.

E) Temporal rate modulation of cue cells. Interaction $F_{2,186}$ = 0.65, P = 0.52; Day $F_{2,186}$ = 3.95, *P=0.021; Treatment $F_{1,186}$ = 14.06, **P = 0.0002; 2-way ANOVA. Planned comparisons: Ctrl: *$P_{Day1\ –\ Day7}$ = 0.032; IR: $P_{Day1\ –\ Day7}$ = 0.93, Tukey's post hoc test. $N_{Ctrl\text{-}Cue}$=39, $N_{IR\text{-}Cue}$=29 cells. Error bars, ± sem.

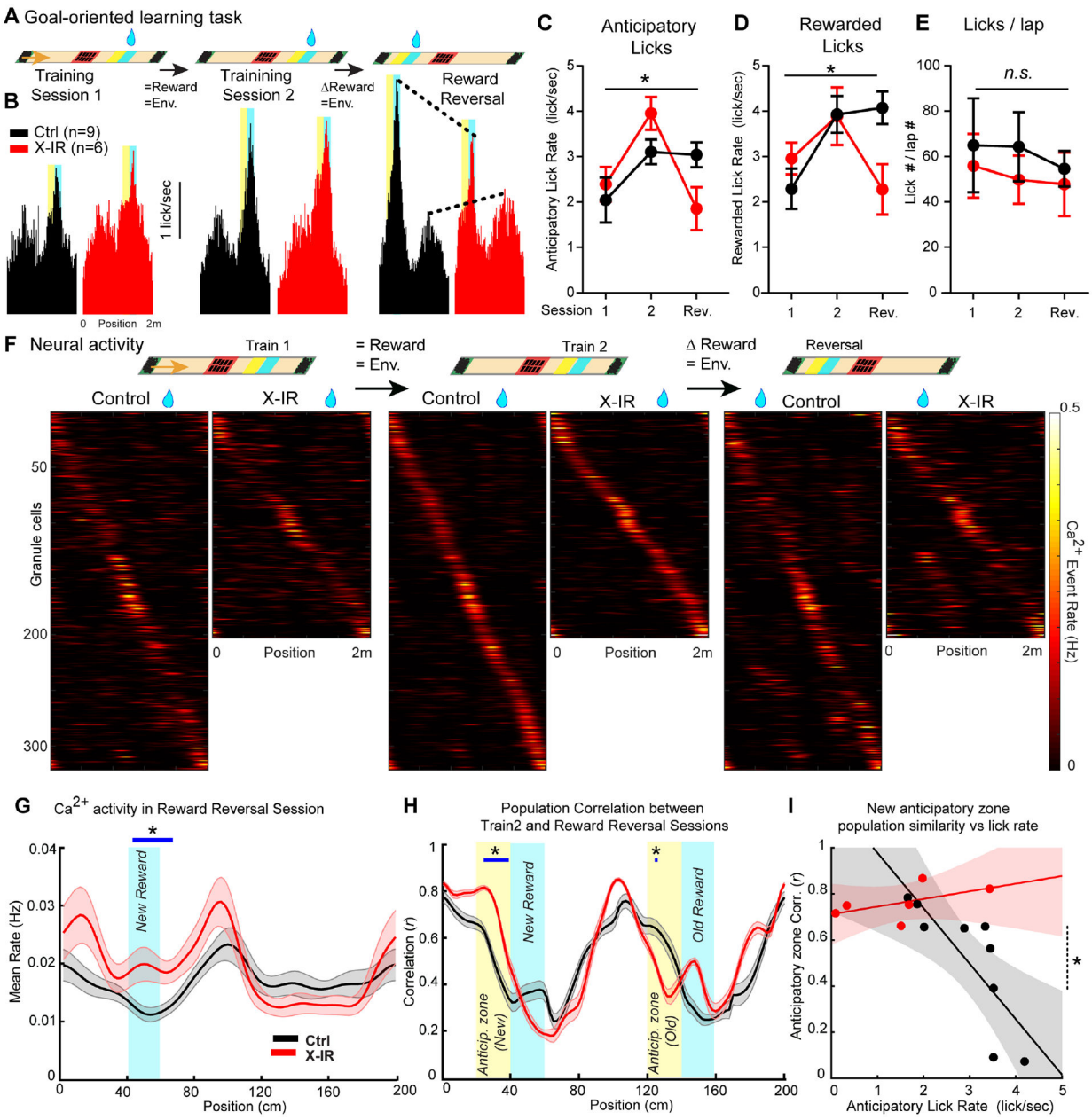

Figure 6. Behavioral impact of impaired mGC remapping in the absence of abGCs.

A) Experimental schematic of the goal-oriented learning task.

B) Averaged lick rate by position histograms. N_{Ctrl}=9, $N_{X\text{-}IR}$=6 mice (Scale bar=1 lick/sec).

C) Lick rates within the anticipatory zone (yellow bands in panel A) in control and X-IR mice. Interaction of Session vs Treatment $F_{2,26}$ = 5.044, *P = 0.014; Session $F_{1.46,19.02}$ = 8.54, **P=0.0044; Treatment $F_{1,13\ 0.03}$, P = 0.84. Reversal session, $P_{Ctrl-IR}$ =0.238.

D) Lick rates within the reward zone (blue bands in panel A). Interaction of Session vs Treatment $F_{2,26}$ = 3.62, *P = 0.0411; Session $F_{1.99,25.94}$ = 4.16, *P=0.0272; Treatment $F_{1,13}$=1.26, P = 0.282; Reversal, $P_{Ctrl-IR}$ =0.069.

E) Total number of licks normalized to number of laps. Interaction of Session vs Treatment $F_{2,26}$ = 0.123, P = 0.88; Session $F_{1.63,21.31}$ = 0.68, P=0.48; Treatment $F_{1,13}$=0.26, P = 0.61. C-E: 2-way ANOVA mixed effects model, Bonferroni's multiple comparisons test.

F) GC activity during the goal-oriented learning task in control and X-IR mice.

G) Averaged spatial firing rates by position for GCs in control and X-IR mice shown in panel "F" on reward reversal session 3. Blue shaded area: new reward location. Blue line: *$P_{Ctrl-IR}$ < 0.05.

H) PV correlations of GCs between the 2nd and reversal session in control and X-IR mice shown in panel F. Blue shaded areas indicate the new (left) and the old (right) reward locations. Blue lines: $P_{Ctrl-XIR}$ < 0.05. G,H : Mann-Whitney test for each 2cm bin between groups. Error bars, ± sem.

I) For each mouse, GCs mean PV correlations within the anticipatory zone is plotted against the anticipatory lick rates in control and X-IR mice. Pearson's R_{Ctrl}=−0.7970, P_{Ctrl}=0.0101, R_{X-IR}=0.5428, P_{X-IR}=0.2657, *$P_{Ctrl-IR}$ = 0.0163, Fisher Z test. See also Figure S5.

KEY RESOURCES TABLE

REAGENT or RESOURCE	SOURCE	IDENTIFIER
Antibodies		
goat anti-Doublecortin	Santa Cruz Biotechnology	sc-8066
chicken anti-EGFP	Aves Labs	GFP-1020
rabbit anti-DsRed	Takara	632496
Alexa488 Donkey Anti-Chicken	Jackson Immunoresearch	703–545–155
Alexa594 Donkey Anti-Goat	Jackson Immunoresearch	705–585–147
Alexa594 Donkey Anti-Rabbit	Jackson Immunoresearch	711–585–152
Bacterial and Virus Strains		
pAAV.Syn.GCaMP6s.WPRE.SV40 (AAV1)	Addgene	100843-AAV1
pGP-AAV-syn-jGCaMP7s-WPRE (AAV1)	Addgene	104487-AAV1
Chemicals, Peptides, and Recombinant Proteins		
NaCl	Sigma Aldrich	S9888
KCl	Sigma Aldrich	P9333
NaH2PO4	Sigma Aldrich	S8282
NaHCO3	Sigma Aldrich	S6014
MgCl2	Sigma Aldrich	M1028
CaCl2	Sigma Aldrich	21115
Na-EGTA	Millipore Sigma	E8145
HEPES	Millipore Sigma	54457
ATP	Millipore Sigma	A1852
GTP	Millipore Sigma	GE27–2076–01
clozapine-N-oxide	Enzo Sciences	BML-NS105–0025
Tamoxifen	Millipore Sigma	T5648–1G
Normal Donkey Serum	Jackson Immunoreseach	017–000–121
Isolfurane		
Ketamine	Zoetis	10004027
Xylazine	Dechra Veterinary Products	ROMP100–50
Isoflurane	Piramal	0010250P
Deposited Data		
Experimental Models: Organisms/Strains		
Mouse: Controls and X-IR mice: C57BL/6J	The Jackson Laboratory	000664
Mouse: Ascl^{CreER}: *Ascl1$^{tm1.1(Cre/ERT2)Jejo}$*/J	The Jackson Laboratory	012882
Mouse: hM4Di$^{F/F}$: B6;129S6-*Gt(ROSA)26Sor$^{tm9(CAG-mCherry,-CHRM4*)Dym}$*/J	The Jackson Laboratory	029040
Mouse: TdTomato$^{F/F}$: B6.Cg-*Gt(ROSA)26Sor$^{tm9(CAG-tdTomato)Hze}$*/J	The Jackson Laboratory	007909
Software and Algorithms		
Python 3	Python Software Foundation	https://www.python.org

REAGENT or RESOURCE	SOURCE	IDENTIFIER
MATLAB	Mathworks	https://www.mathworks.com
Suite2p	Carsen Stringer, Marius Pachitariu	https://www.suite2p.org/
Cellpose	Carsen Stringer, Marius Pachitariu	https://www.cellpose.org/
Prism	GraphPad	https://www.graphpad.com/